NANO-ELECTROMECHANICAL ACTIVE RESONANT DEVICES

by

Alireza Ramezany


APPROVED BY SUPERVISORY COMMITTEE:

Siavash Pourkamali, Chair

Jeong-Bong Lee

Wenchuang (Walter) Hu

Chadwin D. Young

This dissertation is dedicated to my parents, who inspired me to pursue my dreams with their continuous support and sacrifice.

# NANO-ELECTROMECHANICAL ACTIVE RESONANT DEVICES

by

ALIREZA RAMEZANY, BS

DISSERTATION

Presented to the Faculty of

The University of Texas at Dallas

in Partial Fulfillment

of the Requirements

for the Degree of

DOCTOR OF PHILOSOPHY IN

ELECTRICAL ENGINEERING

THE UNIVERSITY OF TEXAS AT DALLAS

December 2018

# ACKNOWLEDGMENTS

First and foremost, I would like to express my deepest appreciation and gratitude to my Ph.D. advisor and mentor Dr. Siavash Pourkamali for his guidance and invaluable support. With his unique intellect and his unwavering conviction in the value of scientific intuition, he has truly inspired me. I would also like to thank my committee members Dr. J.B Lee, Dr. W. Hu and Dr. C. Young for their insightful comments and suggestions.

I would like to acknowledge my friends and colleagues Dr. Varun Kumar, Keith Hernandez, Dr. Mohamad Mahdavi, Dr. Emad Mehdizadeh, Amin Abbasalipour and Vahid Qaradaghi for their valuable discussions and cooperation. I also want to thank the cleanroom staff at The University of Texas at Dallas who did their best to keep the equipment running all the time.

Last but not least, I wish to thank my dear father and mother, who have made great sacrifices for me to be where I am. They have been a constant source of emotional support and inspiration for many years away from family.

July 2018

NANO-ELECTROMECHANICAL ACTIVE RESONANT DEVICES

Alireza Ramezany, PhD
The University of Texas at Dallas, 2018

Supervising Professor: Siavash Pourkamali, PhD

Over the last three decades, various functionalities ranging from frequency selection and timing to sensing and actuation have been successfully demonstrated for microscale and nanoscale electromechanical systems. Although such capabilities complement solid-state electronics, enabling state-of-the-art compact and high-performance electronics, the amplification of electronic signals is an area where micro-/nano mechanics have not experienced much progress.

On the other hand, channel-selective filtering and amplification in ultrahigh-frequency (UHF) receiver front-ends are crucial for the realization of cognitive radio systems and the future of wireless communication. In the past decade, there have been significant advances in the performance of microscale UHF electromechanical resonant devices. However, such devices have not yet been able to meet the requirements for direct channel selection at RF. They also occupy a relatively large area on the chip making implementation of large arrays to cover several frequency bands challenging.

The main objective of this work is to demonstrate amplification of electrical signals using a very simple nanomechanical device occupying a very small footprint without using solid state transistors. It is shown that vibration amplitude amplification using a combination of mechanical

resonance and piezoresistive internal amplification can turn the relatively weak piezoresistivity of silicon into a viable electronic amplification mechanism. With its inherent frequency selective nature, such mechanism can also address the need for ultranarrow-band filtering along with the amplification of low power signals in wireless communications and certain sensing applications.

Finally, using the presented electromechanical model and the fabricated nano-scale devices it is demonstrated that the performance of the proposed nano-electromechanical active resonant devices improves significantly as the dimensions are reduced to the nanoscale, presenting a potential pathway toward deep-nanoscale electronics.

TABLE OF CONTENTS

ACKNOWLEDGMENTS……..……..v

ABSTRACT…….…..vi

LIST OF FIGURES…….…x

LIST OF TABLES…….…xv

CHAPTER 1 INTRODUCTION…….……..1

1.1 Overview…….…..…...1

1.2 Ultra-High Frequency RF MEMS Resonators……..…..…..2

CHAPTER 2 INTERNAL AMPLIFICATION IN THERMAL PIEZORESISTIVE RESONATORS…….…..5

2.1 The Piezoresistive Effect…….....….5

2.1.1 Fundamentals of Elasticity and Piezoresistivity…….6

2.2 Piezoresistor: A Natural Transistor…….…8

2.3 Mechanical Resonance……..10

2.3.1 Thermally Actuated Piezoresistive Resonator……...15

2.4 Internal Amplification……18

2.4.1 Linear Model at Resonance……..21

2.4.2 Effects of Scaling…….……..26

CHAPTER 3 ELECTROMECHANICAL ACTIVE RESONANT DEVICES …….…….28

3.1 Active Resonant Devices Fabricated using FIB……28

3.2 Validation of scaling theory…….……..34

3.3 Ultrahigh Frequency Nanomechanical Piezoresistive Amplifiers…….……39

3.3.1 Comprehensive Electrical Model…….……..40

3.3.2 Figure of Merit……...50

3.3.3 Comparison to State-of-the-art……..52

3.4 Discussions and Future Work……53

CHAPTER 4 SIDE PROJECTS……..56

4.1 Piezoelectric Micro-Resonators for High-Resolution Gas Flowmetry……..56

4.2 Frequency Modulated Electrostatically coupled Resonators for Sensing Applications……...66

REFERENCES……..74

BIOGRAPHICAL SKETCH…….80

CURRICULUM VITAE

LIST OF FIGURES

Figure 2.1. (a) A general description of a transistor, in which the gate voltage can modulate the output current. (b) A piezoresistor can behave similarly to a transistor. If coupled with a DC source, input stress can modulate the output current. (c) In order to control the current in a piezoresistor by an input voltage, an electromechanical actuator must be used. .....9

Figure 2.2. (a) Mass-spring equivalent of a resonant system with a single degree of freedom (b) Frequency response of a mass-spring system .....13

Figure 2.3. Ideal frequency response of a mass-spring resonator showing the rapid phase change within the -3dB bandwidth.....14

Figure 2.4. (a) Equivalent RC circuit describing the frequency dependence of temperature distribution in a thermally conductive beam. (b) Thermal frequency response of a thermally conductive beam .....16

Figure 2.5. (a) As the fluctuating input AC power decreases, the piezoresistive beam contracts as a result of its decreasing temperature and therefore longitudinal stress. (b) Increasing the fluctuating input power causes the piezoresistive beam to expand due to Joule heating and therefore thermal expansion.....17

Figure 2.6. The internal amplification. (a) Additional force toward compression as the piezoresistive beam expands and cools concurrently due to the reduction in the piezoresistor value, when biased with a constant DC bias current. (d) Additional force towards expansion as the beam contracts due to an increase in the resistance and therefore the internal heat……..19

Figure 2.7. A schematic view of the internal amplification. If the mechanical resonance frequency is chosen to be sufficiently larger than the thermal cut-off frequency, the output vibration will be 180º out of phase with the input power. When supplied with a DC current a negative piezoresistive coefficient can form a 0º loop phase. In this manner the device can absorb power from the DC source and increase the vibration amplitude.....20

Figure 2.8. Electrical model and behavior in response to DC bias current. (a) Electrical model of the electromechanical resonant amplifier, consisting of the physical resistance of the piezoresistive beam ($R_A$) in parallel with the RLC components, in which $r_m$ is the motional resistance with negative value for a beam with a negative piezoresistive coefficient, $L=Q_m r_m/\omega_0$, and $C=1/(Q_m r_m \omega_0)$. At the resonance frequency $\omega_0$, the circuit reduces to the combination of the two resistors: $R_A$, which is the passive component, and $r_m$, which is the active component. (b) Effect of the DC bias current on the overall resistance of the device at resonance frequency. By increasing the bias current and thus $|g_m|$, the device transitions from being a passive element (that is, positive resistance values) to an active element (that is, negative resistance values). (c) Effect of bias current on the voltage gain. At small

currents, the device is passive and thus attenuates the input signal. At marginally higher currents, the device continues to attenuate because the internal amplification is not sufficiently strong to compensate for most of the loss in the system, even though the device is in the active region (blue). At currents larger than $I_{DC}^1$, the device will amplify the input signal because the loss due to physical resistance is compensated for via internal amplification (red). At currents higher than $I_{DC}^2$ when the internal amplification has compensated for all losses in the resonator and the load, the combination will enter the oscillation zone and will become unstable (green). .....23

Figure 2.9. A SEM view of a silicon microstructure used as an electronic amplifier consisting of a 9μm×600nm piezoresistor and two resonating plates. The structure is 4μm thick.....24

Figure 2.10. Test circuit configuration showing bias resistors and coupling capacitors. Effectively, the MEMS device is connected in series with the input resistance of the network analyzer acting as a 50Ω load. .....25

Figure 2.11. Measured frequency responses of the device with different DC bias values. As the bias voltage (and current) increases the peak amplitude increases while sharpening and the device goes from an attenuator to an amplifier, and eventually self-sustained oscillation occurs. .....25

Figure 3.1. SEM images of the nanoelectromechanical amplifier after each fabrication step. (a) Initial shape of the device fabricated on an SOI wafer with n-type doped, 0.04-Ωcm resistivity and 2-μm device layer after patterning of the support beams and a single mass using photolithography followed by deep reactive ion etching (DRIE) and HF removal of the buried oxide layer. (b) The center of the initial single mass is etched from the sides using FIB to form the two suspended masses along with a preliminary wide beam in the middle. (c) The final image of the fabricated device after FIB etching continues with a higher precision to form a 100-nm-wide piezoresistive beam and successive dry thermal oxidation and oxide removal in HF to trim the edges and reduce the beam width to 70 nm. (d) Close-up image of the final beam. (e and f) Close-up image of the beam and the final fabricated device, respectively, of a similar beam with larger masses (75 μm×75 μm), which provide gain at lower frequencies. .....30

Figure 3.2. Measurement setup, showing the connection between the network analyzer and the device. .....31

Figure 3.3. Measured frequency response of the nanoelectromechanical resonant amplifier. (b) amplitude and (c) phase response of a nanoelectromechanical resonant amplifier, operating at 4.2 MHz measured by a network analyzer for a matched load of $R_L=R_A$. By increasing the DC bias current, the device makes the transition from attenuation to amplification and finally to oscillation at the resonance frequency, as predicted in Figure 2.8. At low bias currents, where the device is passive, the phase is zero with an absolute voltage gain of less than one. At the transition from the passive region to the active region, where the device resistance $R_D$ is infinite, it is shown that the gain has the strongest downward peak,

indicating that little of the input signal passes through the device to the load. In the active region, the peak begins to grow towards amplification with a phase of 180°. On the verge of oscillation, the phase becomes zero again, and the system becomes unstable. .....32

Figure 3.4. Measured frequency response of the resonant amplifier with 5μm×5μm mass plates. .....33

Figure 3.5. SEM views of the fabricated devices. The 82 and 162 MHz devices were fabricated using E-Beam Lithography, while the 5 and 10MHz were fabricated by standard photolithography. .....35

Figure 3.6. Measured $S_{21}$ responses of the 5MHz Device with 50 Ohm load under atmospheric pressure .....36

Figure 3.7. $S_{21}$ response of 162MHz, the signal is limited by parasitic capacitances of the measurement setup. .....37

Figure 3.8. Measured frequency response of the nanoelectromechanical resonant amplifier .....38

Figure 3.9. More accurate electromechanical model, in which the physical resistance is in parallel with a frequency dependent motional current source. .....40

Figure 3.10. Equivalent electrical circuit of a mechanical resonator .....42

Figure 3.11. A proper meshing scheme of a nanomechanical resonant device for AC temperature distribution simulation .....43

Figure 3.12. Simulated DC temperature distribution for 1V DC and 10mV AC input with 300K ambient temperature .....44

Figure 3.13. Simulated AC temperature showing the variations in amplitude along the piezoresistor .....45

Figure 3.14. Plots of AC temperature on the nanobeam showing a 45° lag of temperature across the piezoresistor .....45

Figure 3.15. Numerical calculations based on the frequency dependent model using the FEA results. Real part of the device impedance marks the overall resistance of the device at resonance and the active region where gain is .....46

Figure 3.16. (a) Schematic view showing the structure and in-plane resonant mode shape of a nanomechanical piezoresistive amplifier. (b) The patterned device shape including a 50nm wide trench on PMMA using EBL at 20KeV. (c) The Cr hard mask after the lift-off process. (d) Etching the device pattern onto the Si device layer and buffer oxide layer using chlorine-based plasma. (e) Released structure after HF dip. (f, g) Different views of the completed devices with operating frequency of 400 and 750MHz. .....47

Figure 3.17. The measured S21 response of the fabricated devices that include the loading effects of the parasitic elements as well as the 50Ω termination of the network analyzer showing minimal insertion loss with large quality factors. ....48

Figure 3.18. The measured motional transconductance as a function of dc power showing close agreement to the numerical calculation. ....49

Figure 3.19. The measured $S_{21}$ frequency responses of the fabricated devices with loads of 50,150 and 250Ω....50

Figure 3.20. Loop gain, a measure of internal amplification strength plotted vs. DC power consumption for measured devices as well as possible loop gains for a 2.4GHz device. Assuming same material parameters (e.g., $\pi_l$, α, E), the 2.4GHz device shows similar loop gains for a reasonable range of power consumption even with a lower mechanical quality factor. ....51

Figure 4.1. SEM view of the AlN resonator with Sail-Shaped structure designed to operate in its second lateral extensional mode. ....58

Figure 4.2. COMSOL simulation for the 2nd lateral extensional mode of the AlN resonator (a) with no external force and (b) in the presence of a uniform perpendicular force. The displacements are exaggerated for demonstration. ....59

Figure 4.3. Measured frequency response for the 2nd lateral extensional mode of the resonator showing a resonant frequency of 10.2 MHz and quality factor of 700....60

Figure 4.4. Fabrication process for sail-shaped piezoelectric micro-resonator. (a) Deposition of Mo and AlN on 100 SOI wafer. (b) Deposition and patterning of Platinum layer as the top electrode. (c) LPCVD oxide used as the hard mask and covering the wire-bond pads with gold. (d) Etching the AlN and the silicon device layer using ICP and DRIE. (e) Removing the handle layer and the Box layer from the backside. ....61

Figure 4.5. (a) Measured Allan deviation for the oscillator utilizing the MEMS resonator as its frequency reference measured with a sample rate of 10Hz indicating the noise floor of 10-8 can be achieved in less than one minute. (b) Frequency fluctuations of the oscillator measured with sample rate of 10Hz. ....62

Figure 4.6. Cross sectional view of the flow chamber. ....63

Figure 4.7. The measurement setup including the characterization board and flow chamber. ....64

Figure 4.8. Oscillator frequency shift as a function of air flow velocity. ....65

Figure 4.9. Time response of the oscillator to a fixed flow with the velocity of 0.15 m/s applied intermittently for durations of 2, 4 and 6 seconds. Frequency shift of 80Hz in accordance

with Equation 4.1 was achieved regardless of the duration of the flow. Rise and fall time of approximately 20ms was measured with the sample rate of 1 kHz.....65

Figure 4.10. Schematic view of two capacitively clamped-clamped beams. As the modulator beam on the right moves towards or away from the resonant beam, the coupling stiffness $K_C$ is modulated and affects the resonance frequency of the resonant beam. .....69

Figure 4.11. SEM view of Device #2 .....70

Figure 4.12. Measured frequency response of each beam for Device #2. .....71

Figure 4.13. AC measurements in the presence of 30mT DC field. Frequency shifts as a function of AC Lorentz currents are plotted for all devices at various bias voltages. .....72

# LIST OF TABLES

Table 3.1. Table of parameters extracted from the measurement for each device corresponding to Figures 3.3 and 3.4. ..... 34

Table 3.2. Conversion between mechanical and electrical parameters ..... 41

Table 3.3. Comparison of the state of the art microscale UHF electromechanical resonant devices demonstrating the fact that while capacitive and piezoelectric devices share a trade-off between quality factor and insertion loss, the nanomechanical piezoresistive amplifier can achieve unprecedented values for both. ..... 52

Table 4.1. Device dimensions ..... 70

Table 4.2. DC measurements and enhance factor E.F for AC measurements……...73

# CHAPTER 1

# INTRODUCTION[1,2]

## 1.1 Overview

MEMS resonators have drawn the attention of many researchers over the past two decades in hopes of enabling highly integrated on-chip timing and frequency selection. The 'resonant gate transistor' demonstrated in 1967 [1], which is known to be the first MEMS resonator, was an active device that integrated a relatively high mechanical $Q$ of a suspended metallic cantilever within a field-effect transistor (FET). However, the majority of recent research on micromechanical resonant devices has focused on piezoelectric and capacitive resonators that are only passive electrical components.

Recently, efforts were made to further combine the benefits of N/MEMS resonators with FETs. The resonant beam was selectively doped for field effect transduction, which is similar to a FET [2]; flexural beam NEMS resonators were integrated with FinFETs [3]; unreleased resonant body transistors were incorporated with n-channel FETs for piezoresistive sensing [4]; AlGaN piezoelectric transduction capability in combination with 2DEG electron gas at the AlGaN/GaN interface was utilized as the conducting channel for a high mobility field effect transistor [5]; and

---

the motion sensing of a piezoelectric resonator in close proximity to a fabricated silicon nanochannel FET [6].

This study takes such efforts a major step further by taking advantage of the previously demonstrated internal thermal piezoresistive energy pumping [7], which was used primarily to drive self-sustained mechanical oscillation, to reach significantly higher amplification and effective quality factors. Using the proposed method, signal amplification can be delivered through a very simple device that offers extreme miniaturization potential without using field effect technology for readout. These capabilities are vital in numerous areas, such as communication systems and sensing applications. In a superheterodyne structure, for example, the device presented in this study can potentially reduce the number of stages of amplification and filtering that are primarily designed to counter the effects of a low quality factor of on-chip elements. Such a device can also be used at the output of a sensor to reduce the noise using ultranarrow-band filtering and amplifying the signal concurrently to increase the minimum detecting capability of the sensor. In addition to frequency selection, it is shown that scaling down the dimensions into the low nanoscale range can improve the performance of such devices.

## 1.2 Ultra-High Frequency RF MEMS resonators

With the ever-growing number of wireless users and the narrowing gap between supply and demand, one of the biggest imminent challenges in the future of wireless communications is the spectrum crisis [8]. The global efficiency can be greatly improved by systems capable of dynamic frequency spectrum allocation replacing the current fixed spectrum allocation system. For example, in opportunistic spectrum access, an unlicensed secondary user is temporarily

allowed spatial and geographic reuse of a part of the spectrum that normally belongs to a licensed user [8], [9]. Such solutions fall inside the general umbrella of cognitive radio system (CRS), a system able to dynamically and autonomously adapt its operational parameters and protocols and to learn from its previous experiences [10], [11]. CRS utilizes software defined radio (SDR) transceivers that are able to use any available band, adapt to multiple access methods and adaptive modulation schemes [8]. Therefore, the RF transceiver section needs to be particularly flexible. Dependence of the current derivatives of conventional superheterodyne RF front-end architecture on intermediate frequency (IF) hardware does not fit effectively within such requirements. In current configurations, the signal from the antenna must be filtered, amplified, and down-converted to IF before it is sent to an analog-to-digital converter (ADC) [12]. Expansion of such architecture to CRS will require a tremendous increase in the number of such components to cover various frequency bands.

To meet the demands of CRS, direct RF sampling approach has been proposed as the only practical architecture for SDR systems [12], [13]. In direct sampling, the signal chain from the antenna is directly fed to a high-performance RF sampling ADC, thus significantly reducing the complexity of the RF front ends. Ideally, a true SDR would not require any specific front-end hardware between the antenna and the ADC. However, processing a large portion of the spectrum without any filtering would require a wide dynamic range for the ADC leading to impractical ADC power consumptions (e.g., 80 W for GSM network as calculated in ref [13]. A more practical solution is to allow the software to select the desired channel by accessing and enabling a narrow-band ($Q > 30{,}000$) filter in a large filter bank [13]. Currently available RF filters (e.g., SAW and FBAR), do not offer such sharp filtering characteristics [14].

Over the past two decades, micro-electromechanical systems (MEMS) have offered innovative enabling technologies for timing and frequency-selection applications. However, the majority of such efforts have focused on piezoelectric and capacitive resonators that are passive electrical components [15]–[21]. Reaching the required Q for channel selection at RF while minimizing insertion loss has proven to be a formidable challenge. While capacitive resonant devices can offer large Qs they introduce significant loss to the filtered signal (e.g., 50−60 dB [15], [19]). Piezoelectric devices, on the other hand, provide a significantly lower insertion loss but suffer from quality factor (e.g., 500−4000 [16], [17], [22]). There have been recent efforts to develop on-chip active resonant components by integrating field effect transistors (FETs) within electromechanical devices [3], [5], [6], [23], [24]. Such devices have not been able to meet the SDR performance requirements either.

# CHAPTER 2

# INTERNAL AMPLIFICATION IN THERMAL PIEZORESISTIVE RESONATORS[1]

## 2.1 The Piezoresistive Effect

The piezoresistive effect, a unique physical property this work is built upon, has a long history in modern physics. The change in the resistivity of materials due to the applied stress was first reported by William Thomson (Lord Kelvin) in 1856 [25]. Decades later, in early 1930s scientists presented the directional dependence of conductivity on the strain in single crystals, and for the first time, the term *piezoresistivity* was used to distinguish between total fractional changes in resistance and the changes in conductivity due to stress[26]–[28]. Later in the 1950s, it was shown that piezoresistive effect in silicon and germanium is two orders of magnitude larger than in metals [29].

In a semiconductor crystal, the strain produced by an applied stress destroys the symmetry of the lattice. This slightly changes the forbidden bandgap between the degenerate valence bands and different conduction band edges and deforms the curvature of different band type. This causes a change in the number of thermally excited electrons, i.e., number of free electrons that contribute to conduction, and more importantly the effective mobility in different directions [30]. Today, piezoresistive transduction is among the most popular sensing mechanisms in MEMS devices [31]–[38].

---

### 2.1.1 Fundamentals of Elasticity and Piezoresistivity

Electrical resistance ($R$) is directly proportional to the resistivity ($\rho$) and length ($L$) and inversely proportional to the cross-sectional area ($A$) of the structure.

$$R = \rho \frac{L}{A} \tag{2.1}$$

Any change in the electrical resistance can be attributed to changes in the dimensions as well as the resistivity. The relative change in the electrical resistance can be found from Equation 2.2, where $\upsilon$ is the Poisson's ratio and $\varepsilon$ is the strain [39].

$$\frac{\Delta R}{R} = \underbrace{(1 + 2\upsilon)\varepsilon}_{\substack{dimensional \\ change}} + \underbrace{\frac{\Delta \rho}{\rho}}_{\substack{Piezo- \\ resistive}} \tag{2.2}$$

It is often costumery to normalize the relative change in electrical resistance by the amount of strain for a better comparison among different material. This normalized parameter is referred to as the gauge factor ($GF$).

$$GF = \frac{\Delta R}{R} \Big/ \varepsilon \tag{2.3}$$

Since the Poisson's ratio of most material is less than 0.36, the dimensional changes, i.e. the first term in Equation 2.2, account for a gauge factor of less than 1.7 [40]. The second term in Equation 2.2 is very small and therefore negligible for most metals. However, for silicon and germanium that are strong piezoresistors, the relative change in resistivity, i.e. the second term, can be 50-100 times larger than the effect of dimensional changes [40]. That is what distinguishes a piezoresistor from simple conductors.

Since the majority of popular piezoresistors, e.g. silicon, germanium, SiC, are anisotropic materials, their piezoresistive strength strongly depends on the direction of stress as well as the direction of the current flow with respect to crystal orientation. The change in resistance due to the piezoresistive effect in response to stress is also tied to the relationship between the applied stress ($\sigma$) and strain ($\varepsilon$), also referred to as elasticity of the material, which can be described using a fourth rank stiffness tensor ($C$) [41].

$$\sigma_{ij} = c_{ijkl}\varepsilon_{kl} \tag{2.4}$$

Indices *i, j, k,* and *l* denote the orthogonal unit vectors (i.e. 1=x, 2=y, 3=z). For example, $\sigma_{ij}$ refers to the stress component in *j* direction on a plane perpendicular to *i*. For silicon, however, due to symmetry conditions, only three independent components of *C* are required to specify elasticity: $c_{1111}$, $c_{1122}$, $c_{2323}$, which for simplicity are denoted by $c_{11}$, $c_{12}$, $c_{44}$ in Equation 2.5. This notation is mainly used in computer simulations such as finite element analysis (FEA) since such tensor calculations are tedious even after such simplifications.

$$C = \begin{bmatrix} c_{11} & c_{12} & c_{12} & 0 & 0 & 0 \\ c_{12} & c_{11} & c_{12} & 0 & 0 & 0 \\ c_{12} & c_{12} & c_{11} & 0 & 0 & 0 \\ 0 & 0 & 0 & c_{44} & 0 & 0 \\ 0 & 0 & 0 & 0 & c_{44} & 0 \\ 0 & 0 & 0 & 0 & 0 & c_{44} \end{bmatrix}, \quad \begin{matrix} c_{11} = 165.6\ GPa \\ c_{12} = 63.9\ GPa \\ c_{44} = 79.5\ GPa \end{matrix} \tag{2.5}$$

It is often simpler to use a directional constant to relate stress and strain, which is referred to as Young's modulus ($E$), such that:

$$\sigma = E\varepsilon \tag{2.6}$$

Young's modulus for every direction in the crystal can be calculated from the elasticity matrix. For example, for the [100] direction [42],

$$E_{[100]} = c_{11} - 2\frac{c_{12}}{c_{12} + c_{11}}c_{12} = 130\ GPa \tag{2.7}$$

Similar to the representation of elasticity, the fractional change in resistivity can be linked to the stress tensor by a piezoresistive tensor. Generally, four subscripts are needed to describe the piezoresistive coefficients ($\pi$). These subscripts represent the directions of voltage, current, and the two directional stress components. These subscripts are also collapsed and simplified, e.g., $\pi_{1111} \rightarrow \pi_{11}$. For silicon, due to symmetry, we have [43]

$$\frac{1}{\rho}\begin{bmatrix}\Delta\rho_1\\ \Delta\rho_2\\ \Delta\rho_3\\ \Delta\rho_4\\ \Delta\rho_5\\ \Delta\rho_6\end{bmatrix} = \begin{bmatrix}\pi_{11} & \pi_{12} & \pi_{12} & 0 & 0 & 0\\ \pi_{12} & \pi_{11} & \pi_{12} & 0 & 0 & 0\\ \pi_{12} & \pi_{12} & \pi_{11} & 0 & 0 & 0\\ 0 & 0 & 0 & \pi_{44} & 0 & 0\\ 0 & 0 & 0 & 0 & \pi_{44} & 0\\ 0 & 0 & 0 & 0 & 0 & \pi_{44}\end{bmatrix}\begin{bmatrix}\sigma_1\\ \sigma_2\\ \sigma_3\\ \sigma_4\\ \sigma_5\\ \sigma_6\end{bmatrix} \tag{2.8}$$

It is often convenient to examine the piezoresistivity in any arbitrary crystal orientation, therefore a much simpler notation was produced that only requires two coefficients. Longitudinal ($\pi_l$) and transverse ($\pi_t$) piezoresistive coefficients such that

$$\frac{\Delta\rho}{\rho} = \pi_l\sigma_l + \pi_t\sigma_t \tag{2.9}$$

In this notation, the longitudinal and transverse directions are measured along and perpendicular to the current flow. The values of $\pi_l$ and $\pi_t$ can be found using the piezoresistive tensor in Equation 2.8. the details of these calculations can be found in [40], [43], [44].

## 2.2 Piezoresistor: A Natural Transistor

A piezoresistor is an active transducer by nature because it can absorb electrical power from a direct current (DC) bias source and transfer modulated power to a load. Similar to the

current flow in a MOS transistor channel that is controlled by an input gate voltage, the current in a piezoresistor is controlled by its mechanical stress. Therefore, an electrical component very similar to a transistor called the 'electromechanical transistor' can be created by combining a piezoresistor with an electromechanical actuator, turning an input control voltage into a mechanical force (Figure 2.1).

The piezoresistive effect, however, is generally far too weak for such an electromechanical transistor to offer a useful amplification factor (that is, a gain of larger than 1). For example, although the current in a solid-state transistor can be modulated over its full range by only a fraction of a volt, 1 MPa of mechanical stress changes the current in a silicon piezoresistor by less than 0.1%. However, there are two ways to tackle this weakness and create an electromechanical transistor that is capable of significant amplification. One convenient approach to improve the

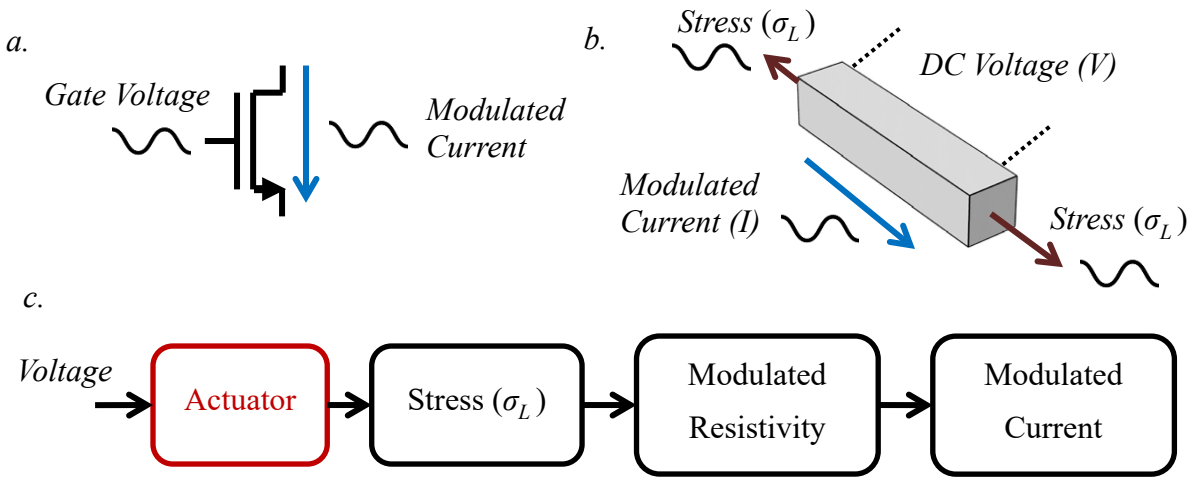


Figure 2.1. (a) A general description of a transistor, in which the gate voltage can modulate the output current. (b) A piezoresistor can behave similarly to a transistor. If coupled with a DC source, input stress can modulate the output current. (c) In order to control the current in a piezoresistor by an input voltage, an electromechanical actuator must be used.

performance of the electromechanical piezoresistive transistor is to use mechanical resonance to

achieve orders of magnitude larger displacements and consequently larger mechanical stress with the same amount of electrically generated input mechanical force. A resonant mechanical structure that is excited into vibration in one of its resonant modes with a quality factor of $Q$ will have a $Q$-times-larger vibration amplitude and therefore stress amplitude compared with when the same structure is subjected to the same force magnitude applied as a constant (that is, DC) force. The second step towards improving this weakness is the internal amplification, in which the vibration amplitude is increased significantly beyond resonance. These two methods will be discussed in the following sections.

## 2.3 Mechanical Resonance

Acoustical resonant systems compile a large portion of MEMS devices as they offer many benefits such as force amplification and frequency selection that are vital to many sensory applications. The simplest requirement of an acoustical resonant system is to have a restoring mechanism that could bring back the system to an equilibrium state in the event that it is slightly pushed out of this resting point (e.g., in response to an external stimulus), and some momentum that can allow the system to be pushed passed the resting point on its way back. Guitar strings are the best example of such a system. When a string is pulled back by the player's fingers, the restoring force of the string makes it vibrate back and forth around its resting state and create a standing wave along the string at its natural (resonance) frequency.

The majority of MEMS resonant systems can be modeled by a one-dimensional spring-mass system as shown in Figure 2.2a, where M, k, and b are denoting the effective mass, effective stiffness and the effective damping coefficient of the system respectively. Even in the presence of

a two-dimensional acoustic wave, often one degree of freedom will tend to dominate around the desired resonance frequency and this model can still be used.

By balancing the forces that act on the mass in Figure 2.2a, a second-order differential equation is reached that can describe the motion of the resonant system in response to an external force.

$$M\ddot{x}(t) + b\dot{x}(t) + k = F(t) \tag{2.10}$$

In general, the solutions to Equation 2.10 can take different forms, however, in most MEMS resonators where the system is underdamped, i.e., $b < 2\sqrt{km}$, the homogeneous solution will take the following form [45]:

$$x(t) = e^{-\xi\omega_0 t}(A\cos\omega_0 t + B\sin\omega_0 t) \tag{2.11}$$

$$\omega_0 = \sqrt{k/M} \tag{2.12}$$

$$\xi = \frac{b}{2\sqrt{kM}} = \frac{1}{2Q} \tag{2.13}$$

Where $\omega_0$, $\xi$, and $Q$ are the resonance angular frequency, the damping ratio and quality factor. The Equation 2.11 suggests that at the resonance frequency (i.e., $f_0 = (1/2\pi) \times \omega_0$), displacement $x(t)$ takes the form of a sinusoidal motion in which the energy oscillated between kinetic and potential form. In addition, in the absence of a sustaining external force, the vibration amplitude decays exponentially according to the damping ratio. Therefore, to have a sustained vibration, the external force $F(t)$ must take a sinusoidal form (i.e., $F(t) = F_0 \sin(\omega t)$).

Considering a steady-state sinusoidal actuating force, the solution to Equation 2.10 can be expressed as [45]:

$$x(t) = A(\omega, \xi)\sin\left(\omega t - \psi(\omega, \xi)\right) \tag{2.14}$$

$$A(\omega, \xi) = \frac{F_0}{k}\frac{1}{\sqrt{\left(1 - \left(\frac{\omega}{\omega_0}\right)^2\right)^2 + \left(2\xi\frac{\omega}{\omega_0}\right)^2}} \tag{2.15}$$

$$\psi(\omega, \xi) = \tan^{-1}\left(\frac{-2\xi\frac{\omega}{\omega_0}}{1 - \left(\frac{\omega}{\omega_0}\right)^2}\right) \tag{2.16}$$

According to Equations 2.14-2.16, the resonant system response depends on the frequency of the actuating force. To simply explain the system response, the frequency spectrum must be divided into three sections:

(1) frequencies well below the resonance frequency i.e., $\omega << \omega_0$, where the Equations 2.14-2.16 will reduce to static Hook's law.

$$\begin{cases} A = \frac{F_0}{k} \\ \psi = 0° \end{cases} \tag{2.17}$$

(2) frequencies in the vicinity of the resonance frequency i.e., $\omega \sim \omega_0$, where the vibration amplitude is amplified by Q times but lags 90º behind the force.

$$\begin{cases} A = \frac{QF_0}{k} \\ \psi = -90° \end{cases} \tag{2.18}$$

(3) frequencies higher than the resonance frequency $\omega > \omega_0$, where eventually the force is changing too fast for the system to react to and the amplitude rapidly drops with an increase in frequency.

$$\begin{cases} A(\omega) \sim \frac{F_0}{k}\frac{{\omega_0}^2}{\omega^2} \\ \psi \sim -180° \end{cases} \tag{2.19}$$

Figure 2.2b shows a qualitative frequency response of a resonant system. In most sensory applications, where force amplification and frequency selection is desired, the resonant system is

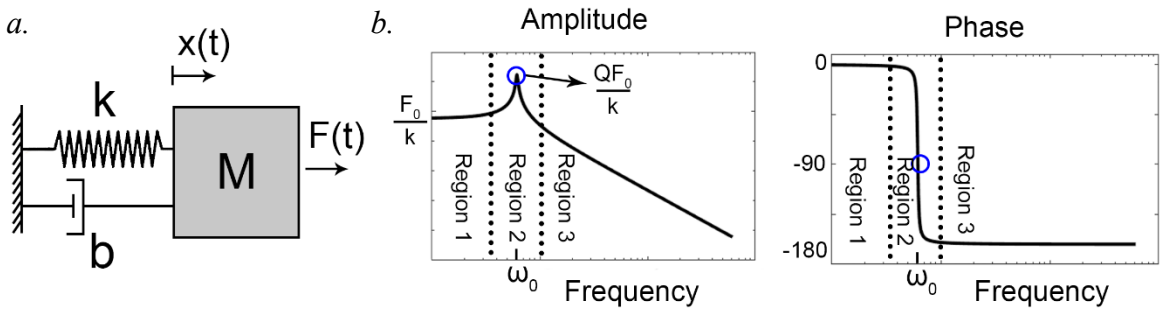


Figure 2.2. (a) Mass-spring equivalent of a resonant system with a single degree of freedom (b) Frequency response of a mass-spring system

operated in the second region near the resonance frequency. Whereas, in many sensors that operate at DC or very low frequencies, such as accelerometers, the resonance frequency is usually considered to be the upper limit of the operation frequency.

It is imperative to discuss the definition and physical meaning of the quality factor presented in Equation 2.13 since this definition is not trivial. The quality factor represents a measure of the efficiency of the resonator in transforming the harmonic excitation into vibration. A common definition of the quality factor is related to the ratio of total mechanical energy in the resonator to the energy dissipated per cycle when excited at its resonance frequency.

$$Q = 2\pi \frac{K.E + P.E}{\Delta W}|_{\omega_0} = 2\pi \frac{\frac{1}{2}kx_{max}^2}{\Delta W}|_{\omega_0} \tag{2.20}$$

In this equation, K.E and P.E represent the kinetic and potential energy of the spring-mass resonator. The total mechanical energy can be also calculated at the maximum displacement where the entire kinetic energy has transformed into potential stored energy. $\Delta W$ is the energy dissipation

per cycle and is equal to the amount of work done by the external force in every cycle. Equations 2.15 and 2.20 yield the result presented in Equation 2.13 where the quality factor is inversely proportional to the damping ratio [45].

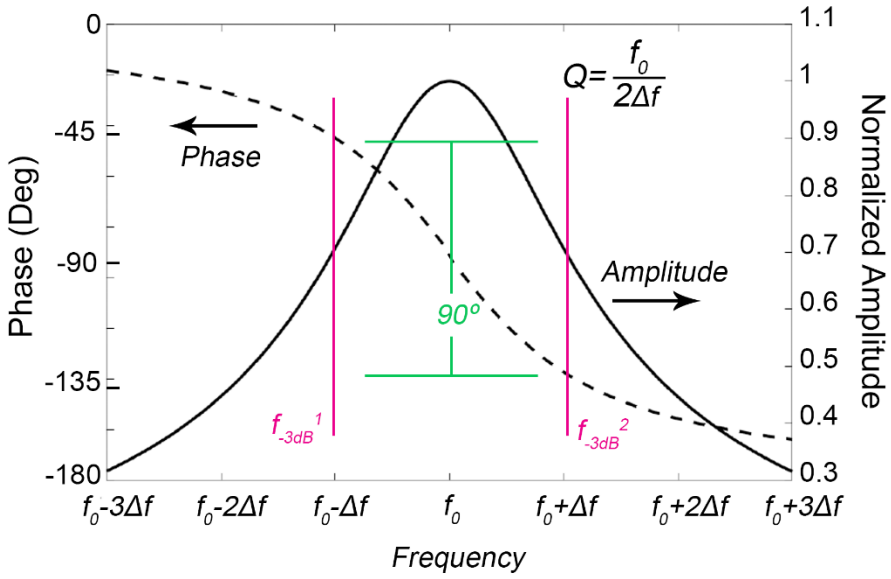


Figure 2.3. Ideal frequency response of a mass-spring resonator showing the rapid phase change within the -3dB bandwidth

Equation 2.20 suggests that at steady state resonance, the resonator stores $Q/2\pi$ times more energy than it loses. This is the reason behind the amplitude amplification at the resonance frequency. From another point of view in the transient state, every cycle the system stores energy equal to the energy it dissipates, and after approximately Q cycles, the stored energy adds up to reach steady state ($1 - e^{-\xi\omega_0\frac{Q}{f_0}} \approx 0.95$). For this reason, resonators are generally slow in transient time. For the same resonance frequency, the higher the quality factor, the slower switch-on time.

In MEMS devices it is often hard to estimate the quality factor by directly examining the displacement value as a function of frequency, or to count the transient cycles in time domain

before the device reaches steady state. One common method to approximate the quality factor is to use the -3dB bandwidth on an output signal that is proportional to displacement. In this method, the frequencies at which the power reaches half of its maximum value (i.e., where the vibration amplitude reaches $1 / \sqrt{2}$ of its maximum) are referred to as -3dB frequencies, or $f_{-3dB}^{1}$ and $f_{-3dB}^{2}$. As shown in Figure 2.3, the quality factor is estimated by the dividing the resonance frequency $f_0$ by bandwidth determined by the -3dB frequencies ($f_{-3dB}^{2}$- $f_{-3dB}^{1}$). Another important aspect of resonance, as shown in this figure, is the rapid phase change near the resonance frequency (almost 90º within the -3dB bandwidth). This figure is valid for any resonator that can be modeled by a mass-spring system and follows the frequency response shown in Equations 2.15 and 2.16.

### 2.3.1 Thermally Actuated Piezoresistive Resonator

In section 2.2 it was shown that if mechanically actuated a piezoresistor can provide an output signal through a change in resistance. However, in addition to providing the output signal, a piezoresistor can also act as a thermal actuator generating the force for excitation of its mechanical resonance via Joule heating. Consider a mere conducting beam that is supplied with an alternating source of power ($P_{AC}$). Upon an increase in the input power level, the beam heats up through Joule heating and consequently expands. On the other hand, once the input power reduces, the beam cools down and shrinks. This alternating temperature ($T_{AC}$) and the resulting periodic strain ($\varepsilon_{AC}$) in a piezoresistive beam can produce a periodic change in the resistance ($R_{AC}$). While the output $R_{AC}$ has the same frequency as the input power ($P_{AC}$), its amplitude and phase in respect to the input depend on the material properties, beam dimensions, and the input frequency.

Modeling the frequency dependent temperature profile of an arbitrary object that is excited through Joule heating can be a complex and daunting task. However, for a current carrying conductive beam that has a large enough length to cross-section ratio so that the heat distribution can be approximated by a one-dimensional system, while the two ends of the beam are kept at a constant temperature, the thermal response can be simplified and represented by an equivalent RC circuit as shown in Figure 2.4. In the thermal domain, temperature and power are equivalent to voltage and current in an electrical circuit. Thermal resistance is defined as $R_{th} = {}^{L}/_{\kappa A}$, where $\kappa$ the thermal conductivity, $A$ the cross-sectional area, and $L$ the length of the beam. Thermal capacitance $C_{th}$ is approximated by $\rho C_H LA$, where $C_H$ and $\rho$ are specific heat capacity and mass density.

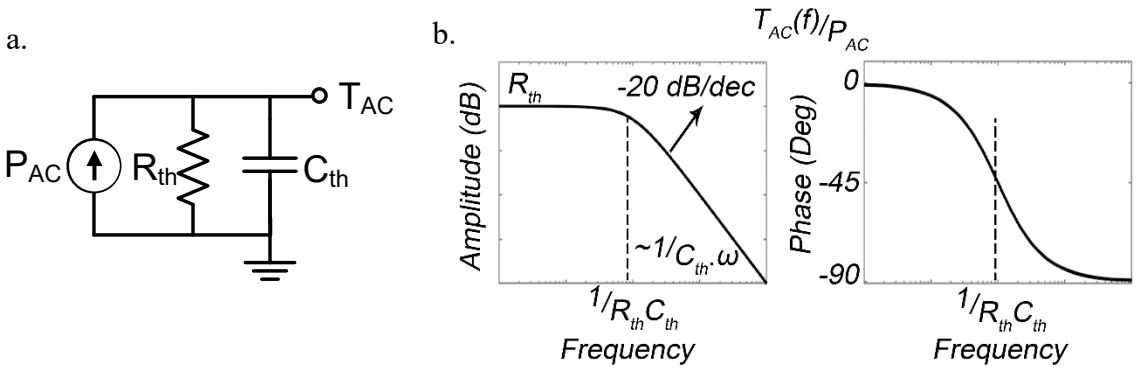


Figure 2.4. (a) Equivalent RC circuit describing the frequency dependence of temperature distribution in a thermally conductive beam. (b) Thermal frequency response of a thermally conductive beam

If the input power fluctuates with a rate slower than the thermal cut-off frequency, i.e.,$1/R_{th}C_{th}$, the temperature will follow the power with the same phase, and the beam acts as a mere thermal resistor. In contrast, when the input power fluctuates much faster than the thermal

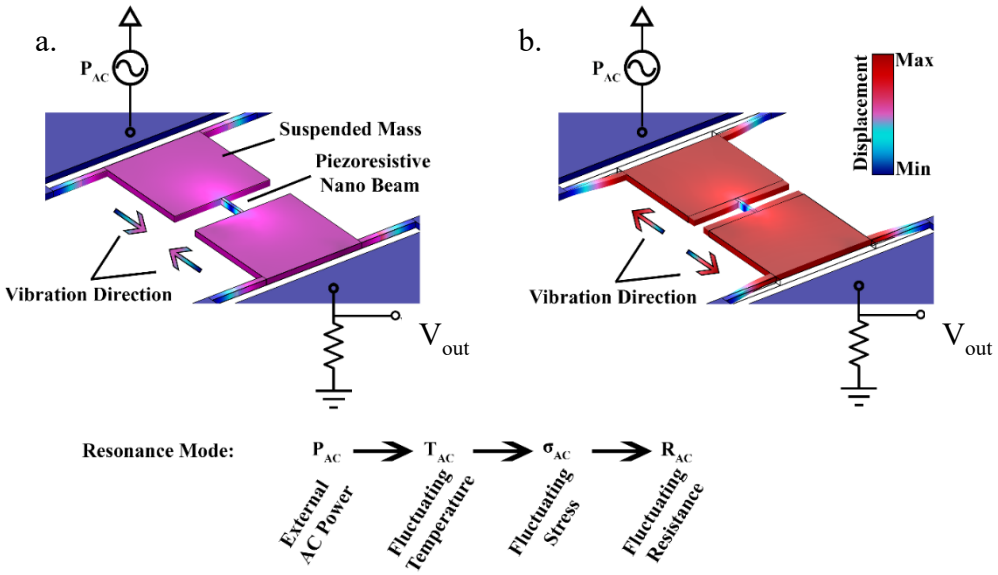


Figure 2.5. (a) As the fluctuating input AC power decreases, the piezoresistive beam contracts as a result of its decreasing temperature and therefore longitudinal stress. (b) Increasing the fluctuating input power causes the piezoresistive beam to expand due to Joule heating and therefore thermal expansion.

cut-off frequency the temperature amplitude reduces significantly and lags behind the power by 90 degrees.

An alternating power supplied at the resonance frequency of the structure can create a relatively large vibration amplitude and therefore a significant stress fluctuation ($\sigma_{AC}$), proportional to the mechanical quality factor of the structure. To control the resonance frequency of the piezoresistor, two relatively large suspended masses must be added to the two ends of the piezoresistor. This lowers the resonance frequency of the overall structure, thus allowing the thermal response of the actuator to have a time constant closer to the mechanical resonance period. The full structure of a thermally actuated resonator with piezoresistive readout is shown in Figure 2.5. In this configuration, a pair of clamped-clamped beams is employed to connect the device to the anchor point and wire-bond/probe pads.

An input AC signal with the frequency of $\omega_{in}$ supplied to actuate the resonator creates an ohmic actuating power with the frequency of $2\omega_{in}$ given that $P=V^2/R$. Therefore, the input signal must have a frequency of one half of the mechanical resonance. To align the input voltage frequency with that of the mechanical resonance, a combination of a DC and AC signals must be applied to the input:

$$P_{in} = \frac{(V_{AC}\cos\omega_{in}t + V_{DC})^2}{R} = \frac{{V_{AC}}^2}{R}\cos^2\omega_{in}t + 2\underbrace{\frac{V_{AC}V_{DC}}{R}\cos\omega_{in}t}_{Actuating\ Term} + \frac{{V_{DC}}^2}{R} \quad (2.21)$$

This also increases the resulting ohmic power significantly.

## 2.4 Internal Amplification

The internal amplification effect, which is the primary focus of this study, originates from the fact that the electrical resistance of the thermal actuator is itself modulated by the vibrations. It is a self-amplifying effect that results from the coupling of the thermal actuation forces and the piezoresistivity of the piezoresistor. The alternating resistance of the piezoresistor $R_{AC}$ created by the external AC power at resonance along with a DC current can create a new source of internal AC power that can amplify the vibration amplitude even further if it is in phase with the externally applied AC power. For this to occur, this additional heating power needs to decrease when the piezoresistor is expanding during resonance so that the actuator begins cooling to help contract the piezoresistor, as shown in Figure 2.6. In the same manner, the piezoresistive heating power created by the DC bias current needs to increase while the actuator is contracting to help the actuator expand again during the next half-cycle, as shown in Figure 2.6. The electrical resistance of a piezoresistor with a negative piezoresistive coefficient (for example, n-type doped single-

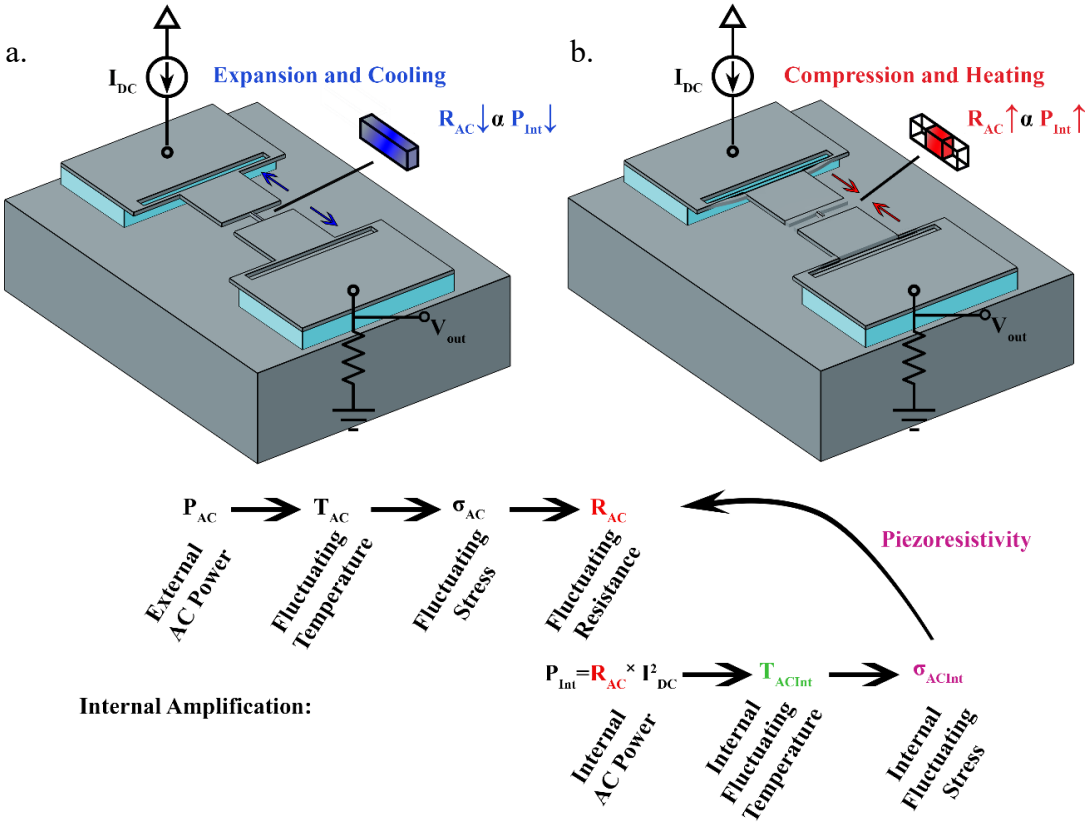


Figure 2.6. The internal amplification. (a) Additional force toward compression as the piezoresistive beam expands and cools concurrently due to the reduction in the piezoresistor value, when biased with a constant DC bias current. (d) Additional force towards expansion as the beam contracts due to an increase in the resistance and therefore the internal heat

crystalline silicon) decreases upon expansion and increases due to compression. Therefore, when biased with a constant current, a negative piezoresistor can provide the correct phase for the internal power ($P_{int} = R_{AC} \times I_{DC}^{\ 2}$) to help amplify the vibration amplitude in the electromechanical resonant amplifier. In this manner, the piezoresistor absorbs energy from the DC bias source and amplifies the mechanical vibration amplitude and, along with it, the stress in the piezoresistor. As a result, the voltage fluctuations across the piezoresistor (that is, the resonant electromechanical amplifier output voltage) will be amplified.

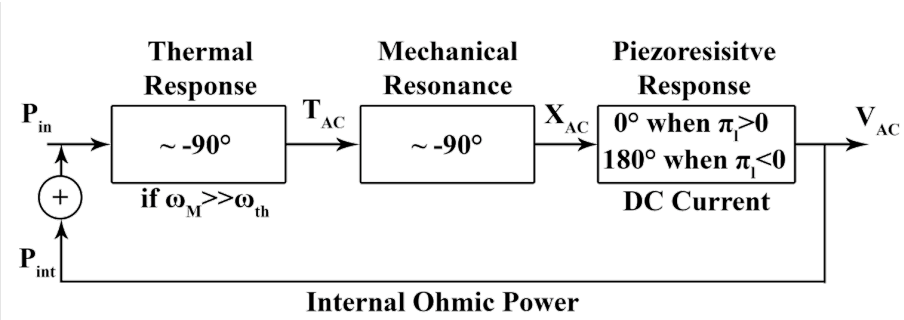


Figure 2.7. A schematic view of the internal amplification. If the mechanical resonance frequency is chosen to be sufficiently larger than the thermal cut-off frequency, the output vibration will be 180º out of phase with the input power. When supplied with a DC current a negative piezoresistive coefficient can form a 0º loop phase. In this manner the device can absorb power from the DC source and increase the vibration amplitude

From a systematic point of view, the device operation can be broken down into three systems: thermal, mechanical and piezoresistive as shown in Figure 2.7. If the mechanical resonance frequency is chosen to be sufficiently larger than the thermal cut-off frequency (i.e., $\omega_M >> \omega_{th}$), the AC temperature will be approximately 90º behind the input power. Subsequently, since the thermal expansion force follows the temperature, the displacement will also be 90º behind the AC temperature. Therefore, the vibration of a thermal piezoresistive resonator under the stated condition will be 180º out-of-phase with the input power. A positive or negative longitudinal piezoresistive coefficient can yield an output power that is out of or in phase with the input power respectively when supplied with a DC current. Since the piezoresistive beam in this configuration plays the role of both the thermal actuator and the piezoresistor at the same time, the resulting AC power from the thermos-electro-mechanical response can actuate the beam in every following half cycle of resonance. For this reason, more DC current that is pumped into the system with a zero loop-phase creates a larger output vibration in response to the same input AC power.

### 2.4.1 Linear Model at Resonance

At resonance frequency, the electromechanical resonant amplifier can be modeled as two parallel elements: a passive resistance that represents the physical electrical resistance of the piezoresistor, and a series RLC tank that represents the motional resonant behavior of the device. In this configuration, the current passing through the RLC tank represents the motional current of the resonant structure or the modulated bias current due to vibration-induced piezoresistive fluctuations. The motional conductance ($g_m$) of the device is defined as the ratio of the motional current to the actuation voltage and can be approximated by Equation 2.22, where $\alpha$, $\pi_l$, $E$, and $Q_m$ are the thermal expansion coefficient, longitudinal piezoresistive coefficient, Young's modulus of the structural material, and the mechanical quality factor of the structure, respectively. In addition, $C_{th}$ is the thermal capacitance of the piezoresistor, $\omega_0$ is the mechanical resonance angular frequency, and $I_{DC}$ is the DC bias current [46]:

$$g_m = \frac{\alpha E \pi_l Q_m I_{DC}^2}{C_{th}\omega_0} \tag{2.22}$$

The motional resistance $r_m$, which is equal to $1/g_m$, can be negative or positive depending on the sign of the piezoresistive coefficient. Figure 2.8a shows the electrical equivalent circuit model of the resonant transistor that can form an electronic amplifier when connected to a load resistance at the output node. At the resonance frequency, the imaginary impedance of the series $L$ and $C$ will cancel each other out, and the model reduces to two parallel resistors: $R_A$, which is the passive physical resistance of the piezoresistor, and $r_m$, which is the negative motional resistance or the active element. At very small DC bias currents, $g_m$ has a small but negative value and increases in magnitude as the current increases. Thus, as the bias current increases, $r_m$, which initially was a

large negative resistor, becomes smaller. Therefore, the overall resistance of the device $R_D$, which is defined as the parallel combination of both physical and motional resistances (that is, $R_D = R_A \,||\, r_m$), depends on the DC bias current. On the basis of the value of $r_m$ with respect to $R_A$, $R_D$ can be negative or positive, as shown in Figure 2.8b. If the motional resistance is greater than the physical resistance, then the overall device resistance has a positive value that is larger than or equal to $R_A$. Therefore, the device behaves as a passive element (that is, positive resistance). In this region, the voltage gain is defined as the voltage transferred from the input to the load resistance $R_L$ through the device and will be positive and smaller than unity; thus, $Gain = R_L/(R_L+R_D)$. As the motional resistance supersedes the physical resistance in magnitude, the overall device resistance becomes negative, and the device becomes active. At this point, the internal amplification effect adds sufficient power to compensate for the power that is lost throughout the physical resistance of the device. However, because $R_D$ remains large, the voltage gain is less than unity, and the input voltage remains attenuated.

Up to this point, the device has been in attenuation mode with regard to the bias current, as shown by the blue color in Figure 2.8. As the bias current increases, the device resistance decreases until it reaches the value of twice the load resistance ($-2R_L$), where the voltage gain becomes unity (Gain = −1). Then, the internal amplification has compensated for all power losses and converts the power it takes from the DC source into a modulated output voltage that is equal to the input; this is the onset of the amplification mode, which is identified by the red color in Figure 2.8. The negative sign in Figure 2.8c represents a 180° phase shift of the signal from the input to the output.

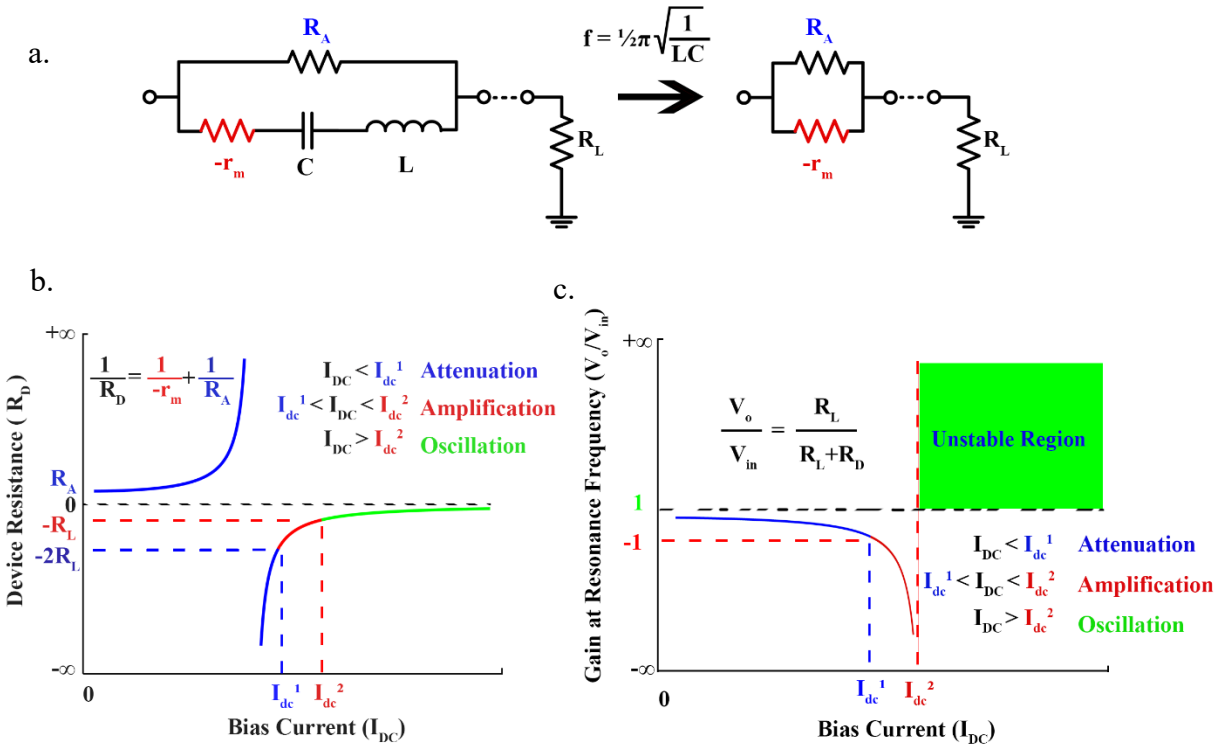


Figure 2.8. Electrical model and behavior in response to DC bias current. (a) Electrical model of the electromechanical resonant amplifier, consisting of the physical resistance of the piezoresistive beam ($R_A$) in parallel with the RLC components, in which $r_m$ is the motional resistance with negative value for a beam with a negative piezoresistive coefficient, $L=Q_m r_m/\omega_0$, and $C = 1/(Q_m r_m \omega_0)$. At the resonance frequency $\omega_0$, the circuit reduces to the combination of the two resistors: $R_A$, which is the passive component, and $r_m$, which is the active component. (b) Effect of the DC bias current on the overall resistance of the device at resonance frequency. By increasing the bias current and thus |gm|, the device transitions from being a passive element (that is, positive resistance values) to an active element (that is, negative resistance values). (c) Effect of bias current on the voltage gain. At small currents, the device is passive and thus attenuates the input signal. At marginally higher currents, the device continues to attenuate because the internal amplification is not sufficiently strong to compensate for most of the loss in the system, even though the device is in the active region (blue). At currents larger than $I_{DC}^1$, the device will amplify the input signal because the loss due to physical resistance is compensated for via internal amplification (red). At currents higher than $I_{DC}^2$ when the internal amplification has compensated for all losses in the resonator and the load, the combination will enter the oscillation zone and will become unstable (green).

As the bias current increases further, the device continues to amplify the signal with larger gains until the device resistance also becomes smaller than the load resistance ($R_D = -R_L$); then,

the internal amplification compensates for all losses throughout the system, including the load. Thus, the overall combination becomes unstable, initiating a self-sustained oscillation. The gain then becomes positive again with a value larger than unity, indicating an amplifying positive-feedback loop (that is, an oscillator). Therefore, the vibration amplitude continues to increase until it is limited by the mechanical saturation of the piezoresistive beam. The oscillation mode is shown in green in Figure 2.8.

In order to clarify the effect of internal amplification on the frequency response when the device makes a transition from attenuation to amplification and oscillation let us briefly examine some measurement results from a device fabricated on 4µm thick N-type silicon as shown in Figure 2.9. In this device, the suspended masses are designed to be 75µm×75µm, and the piezoresistor to be 0.6µm×9µm. The fabrication and measurements will be discussed further in depth in future chapters.

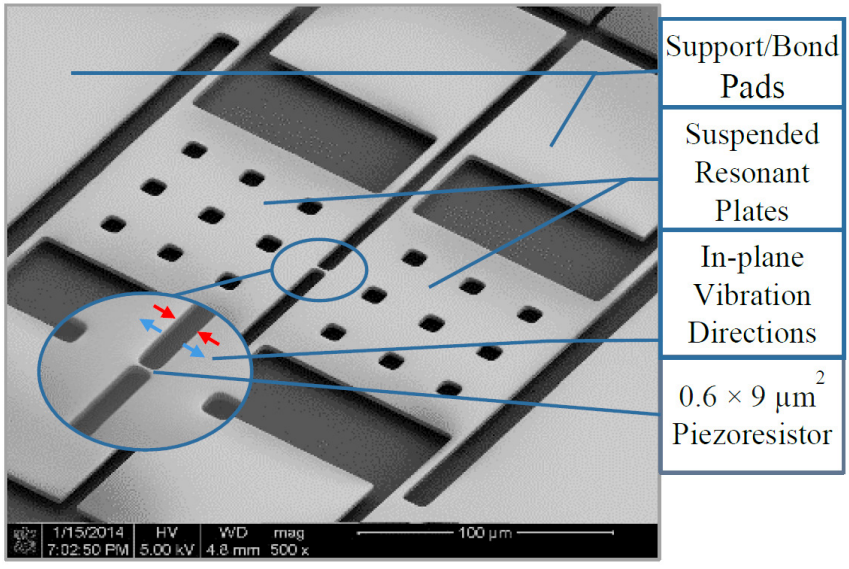


Figure 2.9. A SEM view of a silicon microstructure used as an electronic amplifier consisting of a 9µm×600nm piezoresistor and two resonating plates. The structure is 4µm thick.

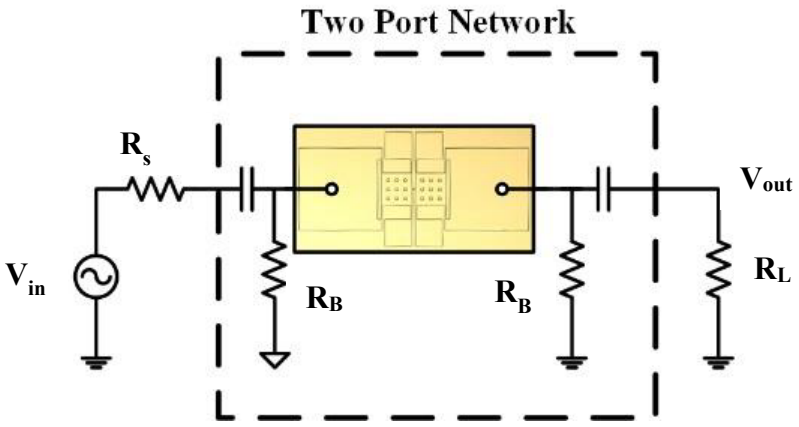


Figure 2.10. Test circuit configuration showing bias resistors and coupling capacitors. Effectively, the MEMS device is connected in series with the input resistance of the network analyzer acting as a 50Ω load

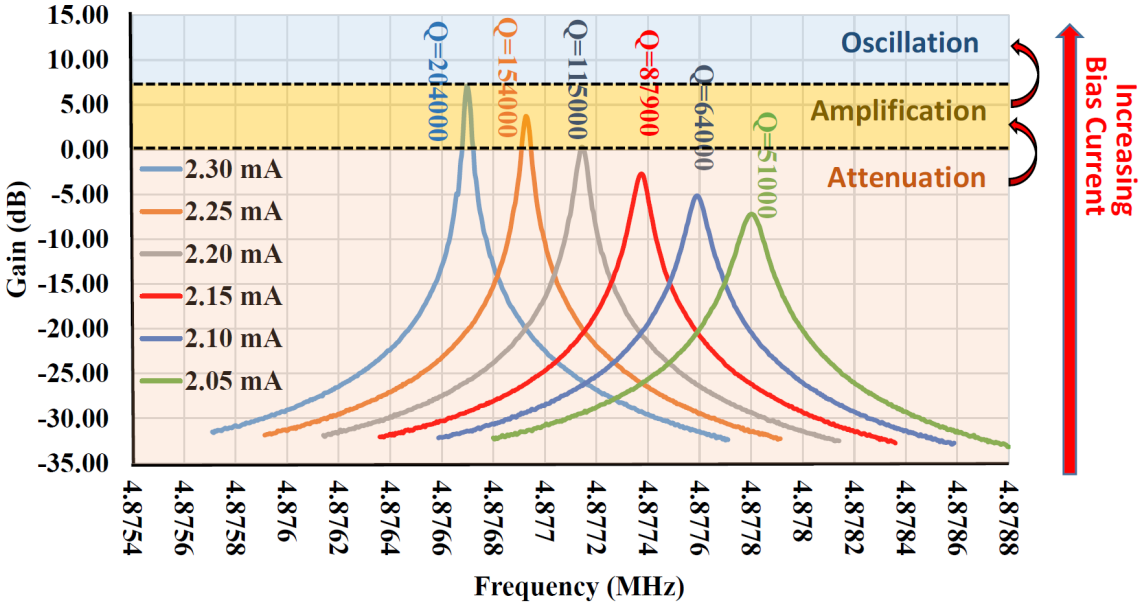


Figure 2.11. Measured frequency responses of the device with different DC bias values. As the bias voltage (and current) increases the peak amplitude increases while sharpening and the device goes from an attenuator to an amplifier, and eventually self-sustained oscillation occurs.

The combination of a DC and AC signals are supplied to and received from the device through a pair of RC filters, while the frequency response is measured as $V_{out}/V_s$ as shown in Figure 2.10.

The measured results depicted in Figure 2.11, suggest that as the bias current increase the resonance peaks rise above the unity gain level, where the device is in the amplification region. Another important implication is the apparent increase in the quality factor along with the gain levels. This is due to the fact that more energy is being stored in the system while the losses remain almost the same. Therefore, the quality factor is strongly correlated with the gain and parameters that determine it such as load and bias current.

### 2.4.2 Effects of Scaling

Lowering the bias current required to maintain the gain of an electromechanical amplifier is critical to its low-power operation. Aside from the overall significance of the desired low-power consumption for any electronic device, a high DC power consumption typically leads to excessive heating and reliability issues, a reduction of the piezoresistive coefficient [47]–[49], and higher levels of thermal and mechanical noise. Therefore, optimization is required for such devices to maintain high levels of gain while lowering the required DC power.

One method to increase the $g_m$ and lower the DC power required is to reduce the electrical resistivity of the piezoresistive beam. If the resistivity is lowered by a factor of $\alpha$, then the bias current can be increased until the $g_m$ is $\alpha$ times larger without changing the DC power consumed in the beam ($P_{DC} \propto \alpha^{-1} R_A \alpha I_{DC}^2$ and $g_m \propto \alpha I_{DC}^2$). Therefore, for the same amount of power, an $\alpha$-times-lower device resistance $R_D$ and consequently a larger gain can be achieved by lowering the resistivity.

However, the most efficient way to optimize the performance of the nanoelectromechanical amplifier is to scale down its physical dimensions. Assuming the piezoresistive coefficient $\pi_l$, the

mechanical quality factor $Q_m$, and Young's modulus $E$ remain constant, the effect of scaling down the device dimensions on $g_m$ can be predicted using Equation 2.23. The transconductance value of the scaled device $g_{ms}$ can be found from Equation 2.23, where $S_L$, $S_A$, and $S_M$, which have positive values less than unity, are scaling factors for the piezoresistive beam length, the beam cross-sectional area, and the suspended masses, respectively. To scale down the device and maintain a constant resonance frequency, the suspended masses must be scaled down by the same factor as the longitudinal stiffness of the piezoresistive beam (that is, $S_M=S_A/S_L$). With this method, Equation 2.23 reduces to $g_{ms} \propto \frac{1}{S_L S_A}$, suggesting that the performance can be improved for a constant frequency.

If the beam length, the area, and masses are scaled down together (that is, $S_L=S_A=S_M=S$), the transconductance $g_{ms}$ will improve by a rate of $S^{-3/2}$, whereas the resonance frequency will increase by a rate of $S^{-1/2}$, indicating that higher transconductance values can be achieved at higher frequencies.

$$g_{ms} = g_m \frac{C_{th}\omega_0}{C_{th}\omega_{0s}} = \frac{\sqrt{S_M}}{S_A\sqrt{S_A S_L}} \tag{2.23}$$

# CHAPTER 3

# ELECTROMECHANICAL ACTIVE RESONANT DEVICES[1,2,3]

In this chapter, the role of internal amplification in realizing electromechanical active resonant devices that can offer narrowband filtering and amplification in very-high and ultra-high frequencies (VHF and UHF) is discussed. Suspended devices are fabricated on SOI wafers using different techniques such as photolithography, Focused Ion Beam (FIB), and Electron Beam Lithography (EBL). The measurements results are compared to the electromechanical model and the scaling prospect. Finally, a more accurate electromechanical is presented to help predict the future designs as the dimensions are scaled down even further.

## 3.1 Active resonant devices fabricated using FIB

As discussed in the previous chapter, having smaller piezoresistor dimensions helps increase the transconductance value or lower the power consumption. FIB can be a useful tool to achieve deep submicron features. However, measures must be taken to increase the throughput and accuracy of the fabrication process. One approach to tackle this problem is to first pattern a

---

[1] This work is licensed under the Creative Commons Attribution 4.0 International License. To view a copy of this license, visit http://creativecommons.org/licenses/by/4.0/ or send a letter to Creative Commons, PO Box 1866, Mountain View, CA 94042, USA. Reference: Ramezany, Alireza, Mohammad Mahdavi, and Siavash Pourkamali. "Nanoelectromechanical resonant narrow-band amplifiers." *Microsystems & Nanoengineering* 2 (2016): 16004.

[2] Reprinted with permission from Ramezany, Alireza, and Siavash Pourkamali. "Ultrahigh Frequency Nanomechanical Piezoresistive Amplifiers for Direct Channel-Selective Receiver Front-Ends." *Nano letters*18.4 (2018): 2551-2556.Copyright 2018 American Chemical Society.

[3] © 2017 IEEE. Reprinted, with permission, from Ramezany, Alireza, et al. "Resonant piezoresistive amplifiers: Towards single element nano-mechanical RF front ends." *Micro Electro Mechanical Systems (MEMS), 2017 IEEE 30th International Conference on*. IEEE, 2017.

preliminary structure that includes large wire-bond pads. Then using FIB, etch the device pattern into the remaining small areas. Here a more detailed description of this method is presented.

Fabrication begins with lithography on a silicon-on-insulator (SOI) wafer composed of a thin silicon device layer that is typically 2-μm thick and is separated from a silicon handle layer by a silicon dioxide thin film that is 2-μm thick. The support beams and a rectangular pattern the size of the overall device are then etched into the device layer using deep reactive ion etching (DIRE). The structure is suspended by removing the underlying insulating $SiO_2$ layer in hydrofluoric acid (Figure 3.1a). At this stage, a preliminary beam is created by etching the initial rectangular shape of the device to create the masses, which are 5μm×5μm, using a focused ion beam (Figure 3.1b). The preliminary beam is then thinned down further to ~ 100 nm, and eventually, the desired beam width of 70 nm is achieved by consecutive dry thermal oxidation and oxide removal in hydrofluoric acid, as shown in Figure 3.1 c and d. The second device with similar beam dimensions that operates at a lower frequency with larger masses (that is, 75μm×75μm) was also fabricated. The SEM image of the second device is shown in Figure 3.1 e and f.

As shown in Figure 3.2, a network analyzer was used to measure the frequency response of the devices. A constant DC current controlled by a voltage source and large bias resistors relative to the device was established through the piezoresistor. The input/output ports of the network analyzer were then connected through the coupling capacitors. Figure 3.3 shows the measured frequency response of the electromechanical amplifier with mass plate dimensions of 4μm×75μm×75μm and beam dimensions of 70 nm× 500 nm× 2μm with a resonance frequency of 4.2MHz. At low bias currents, where the device is operating in attenuation mode and the device

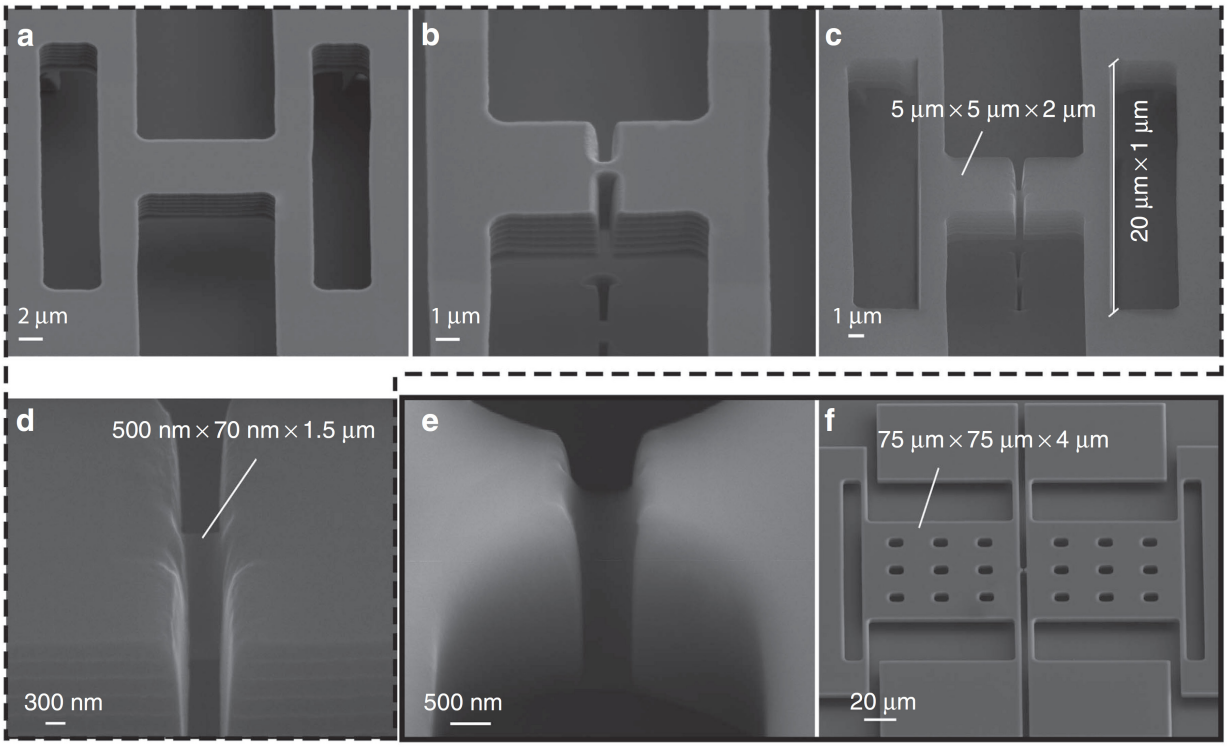


Figure 3.1. SEM images of the nanoelectromechanical amplifier after each fabrication step. (a) Initial shape of the device fabricated on an SOI wafer with n-type doped, 0.04-Ωcm resistivity and 2-µm device layer after patterning of the support beams and a single mass using photolithography followed by deep reactive ion etching (DRIE) and HF removal of the buried oxide layer. (b) The center of the initial single mass is etched from the sides using FIB to form the two suspended masses along with a preliminary wide beam in the middle. (c) The final image of the fabricated device after FIB etching continues with a higher precision to form a 100-nm-wide piezoresistive beam and successive dry thermal oxidation and oxide removal in HF to trim the edges and reduce the beam width to 70 nm. (d) Close-up image of the final beam. (e and f) Close-up image of the beam and the final fabricated device, respectively, of a similar beam with larger masses (75 µm×75 µm), which provide gain at lower frequencies.

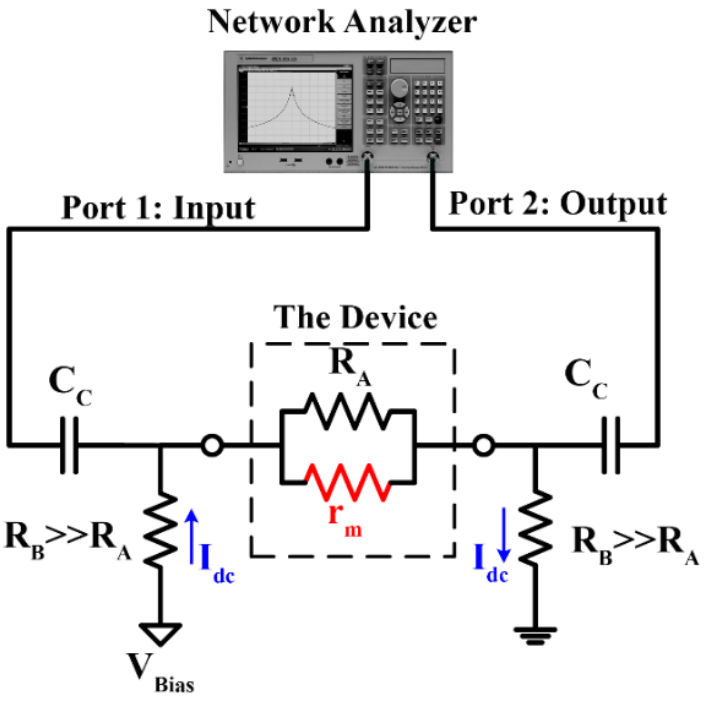


Figure 3.2. Measurement setup, showing the connection between the network analyzer and the device

resistance is positive, the downward peak becomes stronger (that is, more attenuation) because $R_D$ increases at resonance frequency with bias current, while the input-to-output phase change is zero. As the device becomes active but is still in attenuation mode, the downward peak begins to move up in the gain amplitude because the internal amplification compensates for the loss through the physical resistance and delivers more power to the load, while the phase remains 180°.

a.

b.

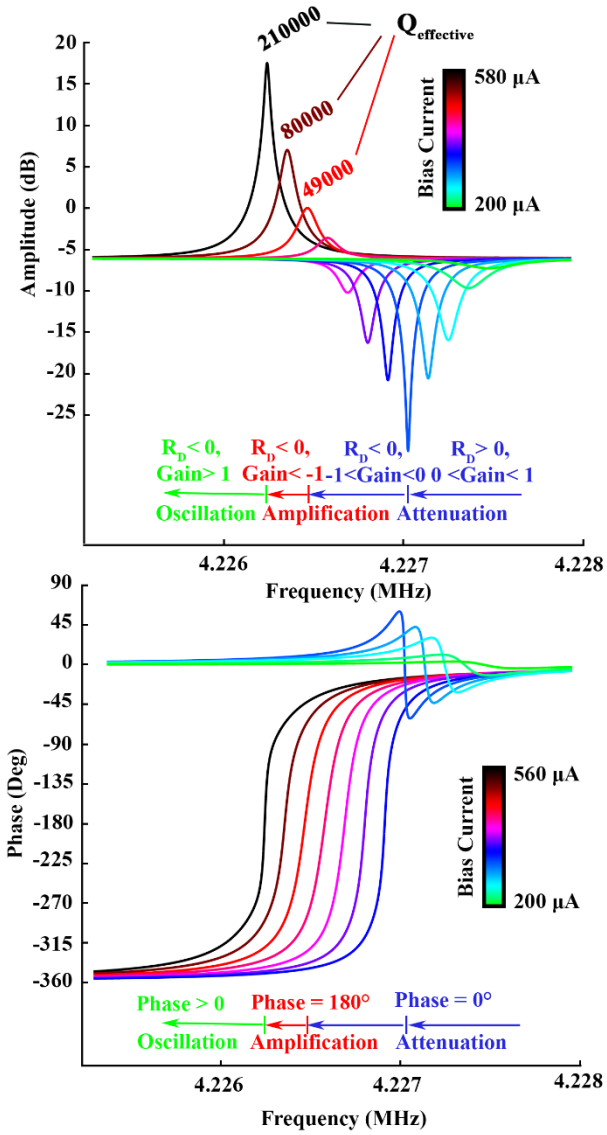


Figure 3.3. Measured frequency response of the nanoelectromechanical resonant amplifier. (a) amplitude and (b) phase response of a nanoelectromechanical resonant amplifier, operating at 4.2 MHz measured by a network analyzer for a matched load of $R_L$=$R_A$. By increasing the DC bias current, the device makes the transition from attenuation to amplification and finally to oscillation at the resonance frequency, as predicted in Figure 2.8. At low bias currents, where the device is passive, the phase is zero with an absolute voltage gain of less than one. At the transition from the passive region to the active region, where the device resistance $R_D$ is infinite, it is shown that the gain has the strongest downward peak, indicating that little of the input signal passes through the device to the load. In the active region, the peak begins to grow towards amplification with a phase of 180°. On the verge of oscillation, the phase becomes zero again, and the system becomes unstable.

As the voltage gain increases, the effective quality factor ($Q_{eff}$), which is also defined as the ratio of the resonant frequency to the −3 dB bandwidth ($f_0 / \Delta f_{-3dB}$), increases. The effective quality factor differs from the mechanical quality factor $Q_m$ used in Equation 2.22. Although the mechanical quality factor, which is defined as the ratio of the mechanically stored energy to the energy lost per cycle, which is also determined by the structural properties of the device, remains constant, an increase in the bias current will result in the compensation for the loss as a product of internal amplification (that is, addition of stored energy created by the electromechanical coupling) and therefore a higher effective quality factor. The increase in the gain at the resonance frequency (that is, a higher peak value) manifests itself in a smaller bandwidth, thereby resulting in a sharper upward peak and a higher effective quality factor.

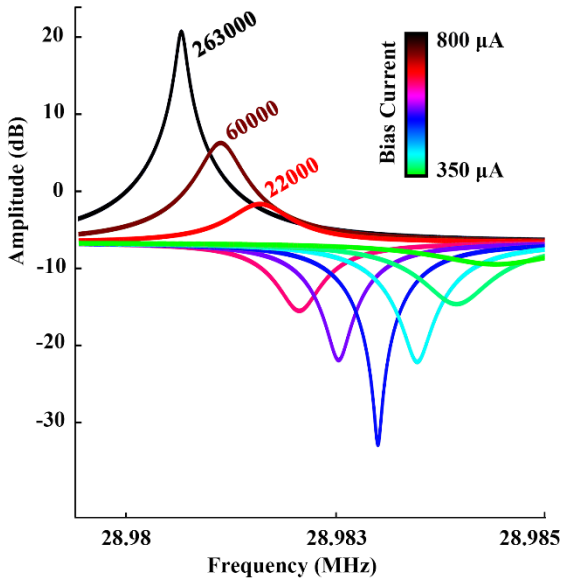


Figure 3.4. Measured frequency response of the resonant amplifier with 5µm×5µm mass plates.

The measured frequency response of the higher-frequency (for example, 30 MHz) electromechanical amplifier with smaller masses of 5µm×5µm×2µm (Figure 3.4) exhibits similar

behavior. As predicted by Equation 2.22, a higher bias current is required to obtain the same gain from a higher frequency device with the same piezoresistor dimensions because a lower mass yields a lower gm when other parameters are held constant.

Table 3.1 shows the parameters obtained from the measurement. In theory, the resonance frequency must remain constant with changes in the bias current. However, as the bias current increases due to increases in DC temperature of the piezoresistor and the temperature dependence of Young's modulus, the stiffness of the beam decreases and leads to a marginal shift of the resonant peak towards a lower frequency.

Table 3.1. Table of parameters extracted from the measurement for each device corresponding to Figures 3.3 and 3.4.

| | $R_A$ (Ω) | 1400 | | | | | | | | |
|---|---|---|---|---|---|---|---|---|---|---|
| 4 MHz Device | $I_{DC}$ (μA) | 200 | 300 | 400 | 440 | 470 | 500 | 540 | 560 | 580 |
| | L (H) | 2.330515 | 1.035808 | 0.58267 | 0.481568 | 0.422073 | 0.372952 | 0.3197614 | 0.2973361 | 0.2771902 |
| | C (F) | 5.97E-16 | 1.34E-15 | 2.39E-15 | 2.89E-15 | 3.30E-15 | 3.73E-15 | 4.35E-15 | 4.68E-15 | 5.02E-15 |
| | $f_0$ (Hz) | 4270390 | 4270280 | 4270060 | 4269840 | 4269620 | 4269510 | 4269290 | 4269180 | 4269070 |
| | $r_m$ (Ω) | -6250 | -2777.778 | -1562.5 | -1291.322 | -1131.734 | -1000 | -857.33882 | -797.19388 | -743.1629 |

| | $R_A$ (Ω) | 2000 | | | | | | | | |
|---|---|---|---|---|---|---|---|---|---|---|
| 29 MHz Device | $I_{DC}$ (μA) | 380 | 500 | 550 | 570 | 600 | 620 | 700 | 750 | 800 |
| | L (H) | 0.253508 | 0.146429 | 0.121018 | 0.112676 | 0.101692 | 0.095239 | 0.0747149 | 0.0650861 | 0.0572056 |
| | C (F) | 1.19E-16 | 2.06E-16 | 2.49E-16 | 2.68E-16 | 2.97E-16 | 3.17E-16 | 4.04E-16 | 4.63E-16 | 5.27E-16 |
| | $f_0$ (Hz) | 28999500 | 28999000 | 28998500 | 28998000 | 28997500 | 28997000 | 28996500 | 28996000 | 28995500 |
| | $r_m$ (Ω) | -4616.805 | -2666.667 | -2203.857 | -2051.913 | -1851.852 | -1734.305 | -1360.5442 | -1185.1852 | -1041.6667 |

## 3.2 Validation of scaling theory

In this section, the validity of scaling theory is put to the test by characterizing and comparing devices operating at different frequencies. Although as shown before using the FIB method to reach deep submicron feature sizes is viable, its low throughput and susceptibility to

ion beam shift during the etch process due to charging stops this method to be effective in producing repeatable and robust high-frequency devices. Therefore, E-Beam lithography was used to fabricate smaller devices.

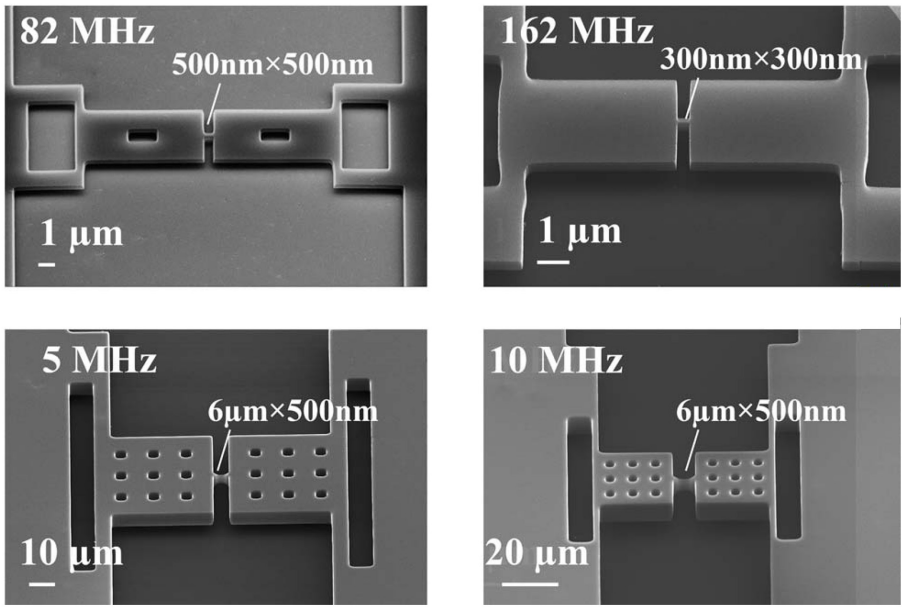


Figure 3.5. SEM views of the fabricated devices. The 82 and 162 MHz devices were fabricated using E-Beam Lithography, while the 5 and 10MHz were fabricated by standard photolithography.

To demonstrate the miniaturization behavior of the devices, a total of four devices were fabricated. Two low-frequency devices operating at 5 and 10 MHz were first fabricated on an SOI substrate, with a 10µm thick device layer and 0.005 Ωcm resistivities. A standard photolithography capable of patterning minimum feature size of 2µm was used to pattern the devices and Si device layer was dry etched by DRIE. Beam dimensions of 6µm×~0.5µm were then achieved via successive steps of dry thermal oxidation and oxide removal in hydrofluoric acid. However, using this method to create smaller beam dimensions is impractical. The thermal oxidation can reduce the width of the beam even down to the nanoscale, but it increases the length of the beam in return. Therefore, to

create beams that are shorter and thinner at the same time E-beam lithography is a more reliable approach. Two more devices with much smaller dimensions and resonance frequencies of 82 and 162 MHz were fabricated on an SOI substrate with 300nm thick device layer and average resistivity of 0.003 Ωcm. To reach deep submicron beam dimensions, E-beam lithography was performed on a 200nm thick 950 PMMA A4 resist. A 25nm Cr was deposited and lifted-off to form a hard mask. Chlorine-based inductively coupled plasma (ICP) etcher was used to dry etch the Si device layer. The SEM images of all devices are shown in Figure 3.5.

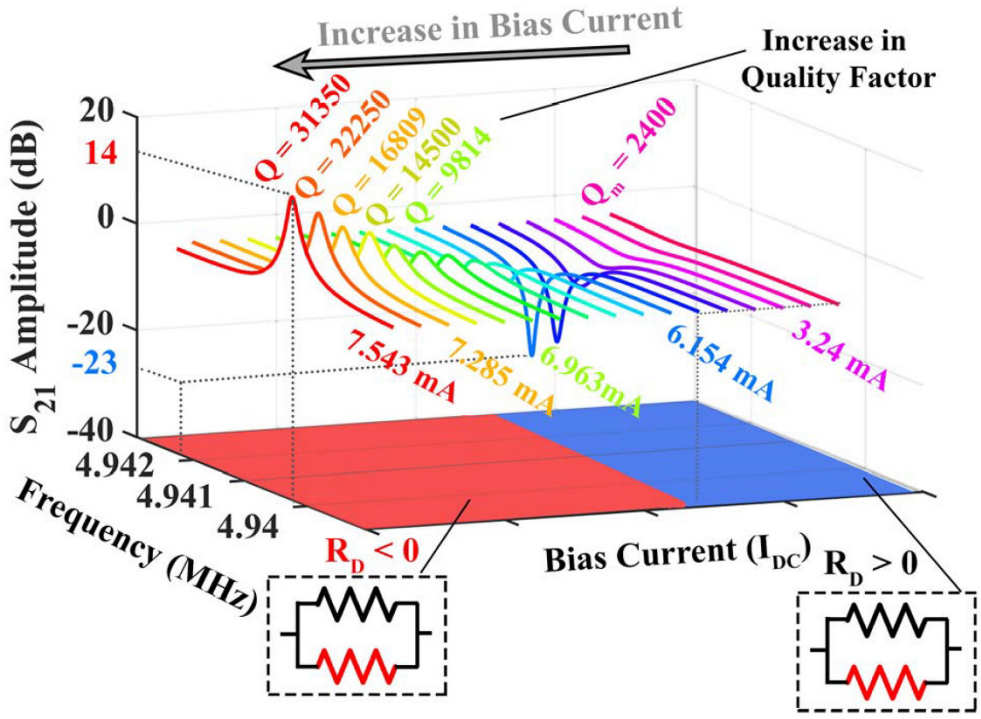


Figure 3.6. Measured $S_{21}$ responses of the 5MHz Device with 50 Ohm load under atmospheric pressure

The changes in the response are monitored for various bias currents. Figure 3.6 shows the measured frequency responses for the 5 MHz devices measured in air, with various bias currents. As predicted in, for low bias currents, the $P_{int}$, the product of internal amplification, is not strong

enough, and the motional resistance is very large in magnitude. Therefore, the device exhibits a passive behavior. As the current increases, the internal amplification intensified and the motional resistance value decreases in magnitude. As a result, a more dominant downward peak is observed. With further increase in the bias current, the motional resistance compensates the passive physical resistance $R_A$ (i.e., $r_m$=$R_A$, and $R_D$ $\rightarrow$-$\infty$), and at the onset of active behavior, a very strong downward peak with 180º phase is attained. From this point forward, with more DC bias current

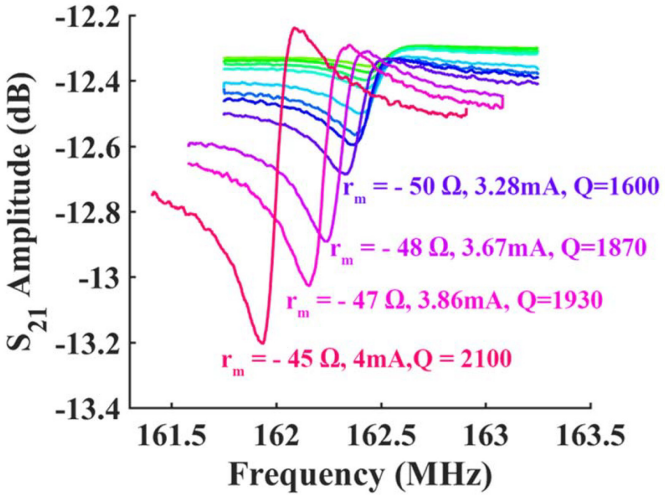


Figure 3.7. $S_{21}$ response of 162MHz, the signal is limited by parasitic capacitances of the measurement setup

pumped into the system, at resonance, the peak surpasses the feedthrough level, and eventually a power gain of unity is reached (i.e., $|R_D| = 2R_L$). The values for the effective quality factor are mentioned in the plot showing the increase in the amount of internal power $P_{int}$, and internal amplification.

Also, it should be mentioned that due to a small raise in DC temperature and reduction in Young's modulus, the resonance frequency slightly shifts towards lower frequencies. Frequency responses of the devices with higher frequencies are expected to follow the same trend. Figure 3.7

shows the frequency response of the 162 MHz device measured under the same conditions. However, in this case, the effects of the parasitic capacitances are much more pronounced.

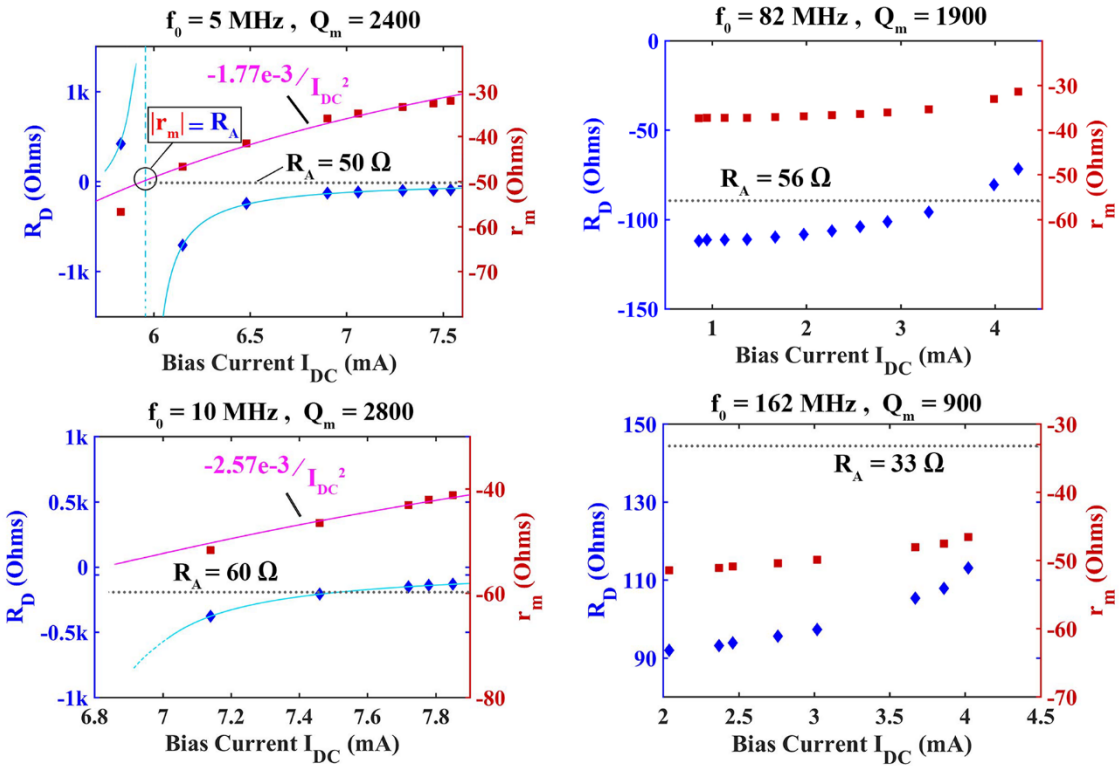


Figure 3.8. Measured frequency response of the nanoelectromechanical resonant amplifier

For a more accurate comparison, the transconductance and motional resistances of all four devices were extracted from the measurements and plotted Figure 3.8. For the device operating at 162 MHz, motional resistances of lower than *-50* Ohms (enough to provide gains for 50 Ohm loads) are achieved similar to those of the 5 MHz devices, but for an almost four times smaller power consumption. This suggests that beam size miniaturization has not only compensated for the increase in frequency but also has improved the $g_m$.

## 3.3 Ultrahigh Frequency Nanomechanical Piezoresistive Amplifiers

Lower frequency versions of resonance piezoresistive amplifiers devices (<160 MHz) have previously been demonstrated. In this section, highly miniaturized nanoscale versions of such devices operating in the UHF range (>0.3 GHz) with significantly reduced power consumption are discussed in detail.

As shown before in theory, scaling down the dimensions of the piezoresistor and masses not only raises the resonance frequency but also reduces the power consumption needed to achieve the same strength of internal amplification. However, as the dimensions shrink, some of the assumptions that were made in the derivation of the model presented in section 2.4.1 start to fail. The foremost assumption in the previous model is neglecting the thermal resistance and capacitances of the suspended masses along with the C-C support beams. When the suspended mass area is significantly small, the AC temperature profile across the piezoresistor no longer resembles that of a long beam with a fixed temperature at each end. For this reason, the AC temperature varies along the length of the piezoresistor. Therefore, each small section of the piezoresistor makes a different contribution to thermal expansion, and a simple thermal *RC* circuit cannot adequately predict the thermal power to expanding force transformation. Time domain finite element analysis (FEA) is a suitable approach to predict the thermal response of a scaled down piezoresistive amplifier.

Additionally, the previous model only holds true at the resonance frequency and fails to predict the device response at other frequencies. Therefore, in this section, a more comprehensive electrical model with the help of COMSOL Multiphysics (FEA to model the thermal response)

will be presented and compared to the measurement results of a nanomechanical piezoresistive amplifier operating in UHF range.

### 3.3.1 Comprehensive Electrical model

As shown in Figure 3.9, the device is modeled as the parallel combination of the beam physical resistance $R_A$, and a frequency dependent motional current source, $i_m\ (f)$, that encompasses the electro-thermo-mechanical coupling that occurs within the piezoresistor. In other words, the voltage across the piezoresistor turns into a mechanically induced electrical current that is fed back to the piezoresistor, and if it has the correct phase it will increase the output voltage.

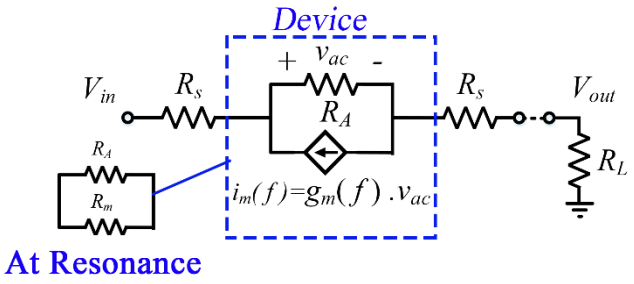


Figure 3.9. More accurate electromechanical model, in which the physical resistance is in parallel with a frequency dependent motional current source

The frequency dependent motional current $i_m$ is related to the AC voltage across the beam by a frequency dependent motional transconductance $g_m\ (f)$.

$$i_m(s) = g_m\ (s).v_{ac} = H_{th}(s).H_M(s).H_{PR} \tag{3.1}$$

Where $H_{th}$, $H_M$, and $H_{PR}$ represent the thermal, mechanical, and piezoresistive transfer functions.

$$H_{th}(s) = \frac{T_{ac}}{P_{ac}} = |H_{th\ avg}| \angle H_{th\ avg} \tag{3.2}$$

The amplitude and phase of the thermal transfer function must be extracted from the FEA simulations. The resulting thermal expansion will generate a force that actuates the mechanical structure, therefore

$$H_M(s) = \frac{X_{th}(s)}{T_{ac}} = \frac{F_{ac}}{T_{ac}} \frac{X_{th}(s)}{F_{ac}} \tag{3.3}$$

Where

$$\frac{F_{ac}}{T_{ac}} = \alpha E A \tag{3.4}$$

And

$$\frac{X_{th}(s)}{F_{ac}} = \frac{1}{Ms^2 + bs + k} \tag{3.5}$$

With *A* as the cross-sectional area of the piezoresistor. The rest of the parameters have been defined in CHAPTER 2. Since the mechanical transfer function resembles the behavior of an RLC circuit, it is convenient to use the following reciprocal table (Table 3.2).

Table 3.2. Conversion between mechanical and electrical parameters

| **Mechanical Parameter** | **Electrical Component** |
|---|---|
| Force | Voltage |
| Displacement | Charge |
| Mass | Inductance |
| Stiffness | Inverse of Capacitance |
| Damping | Resistor |

Figure 3.10 shows the electrical equivalent of the mechanical transfer function $H_M$. Any addition force acting on the device, e.g., Brownian noise, must be incorporated here as an extra voltage source.

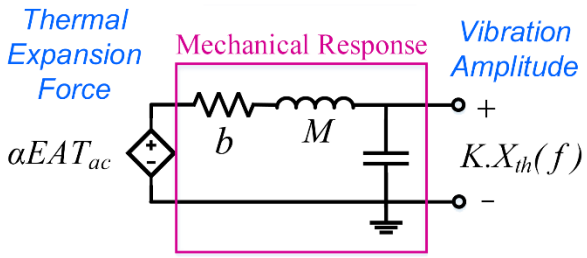


Figure 3.10. Equivalent electrical circuit of a mechanical resonator

As an example, let us consider the following design parameters for a device operating at 750MHz: a 50nm×200nm piezoresistor, 800nm×800nm mass plates, and 600nm×150nm support beams with a 300nm device layer thickness with an electrical sheet resistance of 30Ω/□. As shown Figure 3.11, the device is meshed in such manner to ensure sufficient resolution is maintained in critical areas such as the piezoresistor and the support beams. The two ends of the device are assigned to Terminals 1 and 2. In the time domain to model the input combination of a DC and an AC voltage, the following function is assigned to Terminal 1, while Terminal 2 is grounded.

$$f(t) = u(t[1/s]).V_{dc} + u(t[1/s]).V_{ac}\sin(2\pi f t[1/s]) \tag{3.6}$$

Where *u(t)* refers to a step function with at least two continuous derivatives with a transition zone much smaller than the signal frequency, *f*. As shown in Equation 2.21, such input voltage generates

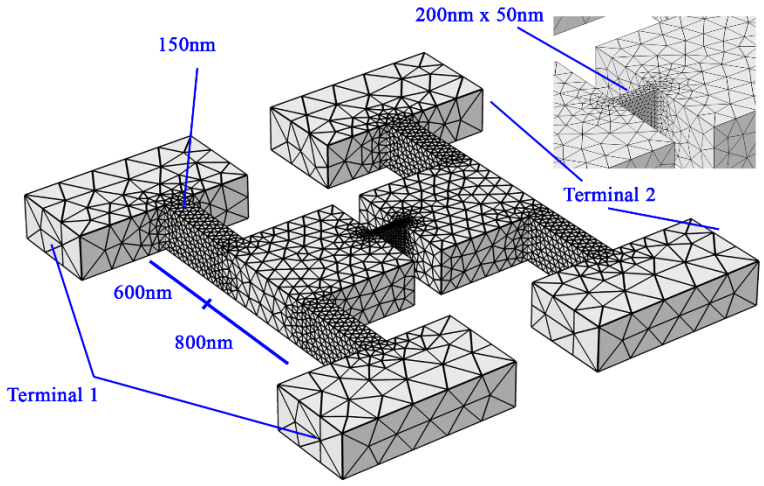


Figure 3.11. A proper meshing scheme of a nanomechanical resonant device for AC temperature distribution simulation

three components of power. Considering a small signal, i.e., $V_{ac}<<V_{dc}$, the DC term usually has the largest value and can affect the temperature-dependent parameters such as Young's modulus, piezoresistive coefficient, and thermal expansion coefficient. The second term if aligned with the resonant frequency will actuate the device. The third term not only is considerably smaller but also will be filtered by the mechanical resonance response and can be neglected. Therefore, to meet the small signal condition $V_{dc}=1$ and $V_{ac}=10mV$ are chosen to simulate the temperature profile in COMSOL Multiphysics.

As shown in Figure 3.12, the temperature at the end of each anchor is fixed at 300K. This assumption is usually valid since the anchor end are connected to large wire-bond/probe pads.

For the given input voltage, a maximum DC temperature of 377K occurs at the piezoresistor.

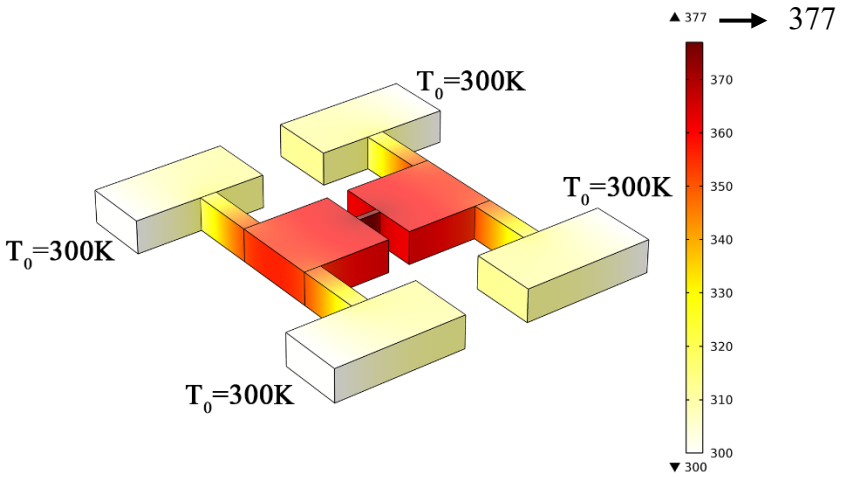


Figure 3.12. Simulated DC temperature distribution for 1V DC and 10mV AC input with 300K ambient temperature.

Figure 3.13 shows the AC temperature profile, which is obtained by subtracting the DC component from the real-time temperature at steady states. It is evident that the AC temperature varies along the piezoresistor. Figure 3.14 shows the time domain plot of the temperature across center and ends of the piezoresistor and the average value compared to the input AC voltage. For this design, the average temperature across the beam lags 45º behind the input power as opposed to the 90º normally assumed for large-scale devices. The amplitude and phase in this plot will help determine the parameters in Equation 3.2.

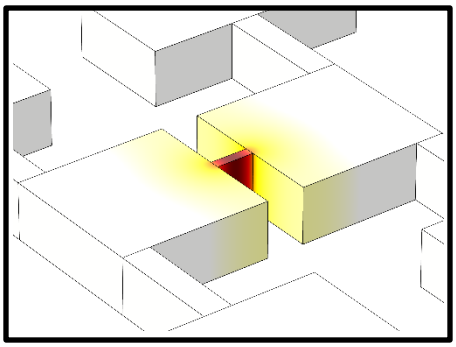

Figure 3.13. Simulated AC temperature showing the variations in amplitude along the piezoresistor

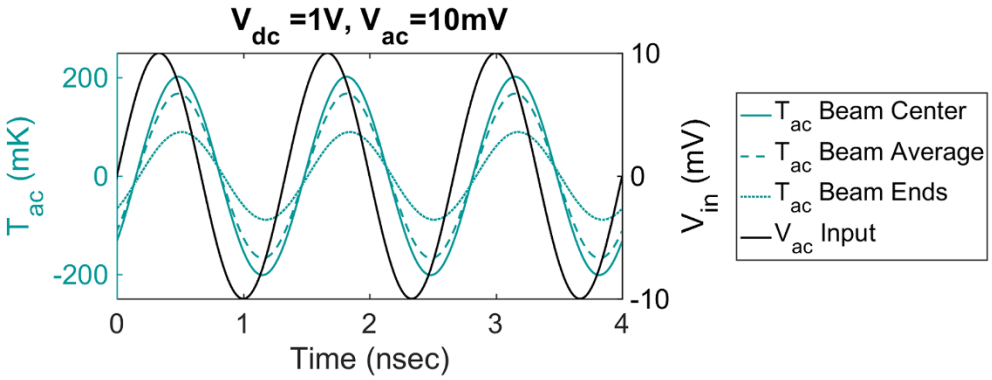


Figure 3.14. Plots of AC temperature on the nanobeam showing a 45° lag of temperature across the piezoresistor.

Figure 3.15 shows numerical calculations of the frequency dependent model using the FEA results and assuming the piezoresistive coefficient ($\pi_l$) of $-10^{-10}\text{Pa}^{-1}$. While the maximum $g_m$ value occurs at $\omega_0$, the internal amplification can only take place at the internal frequency $\omega_1$, where the $g_m$ has zero phase but a smaller magnitude. Figure 3.15b shows the real part of the device impedance $Z_D$ including the overall device resistance $R_D$ at resonance, i.e., $Real(Z_D)|_{@\omega_1}$. Increasing the DC bias current increases the absolute value of $g_m$ at resonance ($\omega_0$ and $\omega_1$), and eventually, the overall device resistance $R_D$ becomes negative. At this point, the $S_{21}$ phase at

resonance changes from 0° to 180°. The device must be matched to the proper load ($R_L$) to provide gain ($Gain = R_L/(R_L + R_D)$). Ideally, the device resistance must satisfy $R_L < |R_D| < 2R_L$ to yield Gain > 1. For a larger load, a smaller $g_m$ and power consumption can maintain the same gain as long as $R_L < |R_D|$. As shown in Figure 3.15d, increasing the DC power further, yields a sharp upward peak with a higher effective quality factor well beyond the initial mechanical $Q_m$ of the resonator. The effective quality factor and maximum signal transmission depend on the value of the load connected to the device.

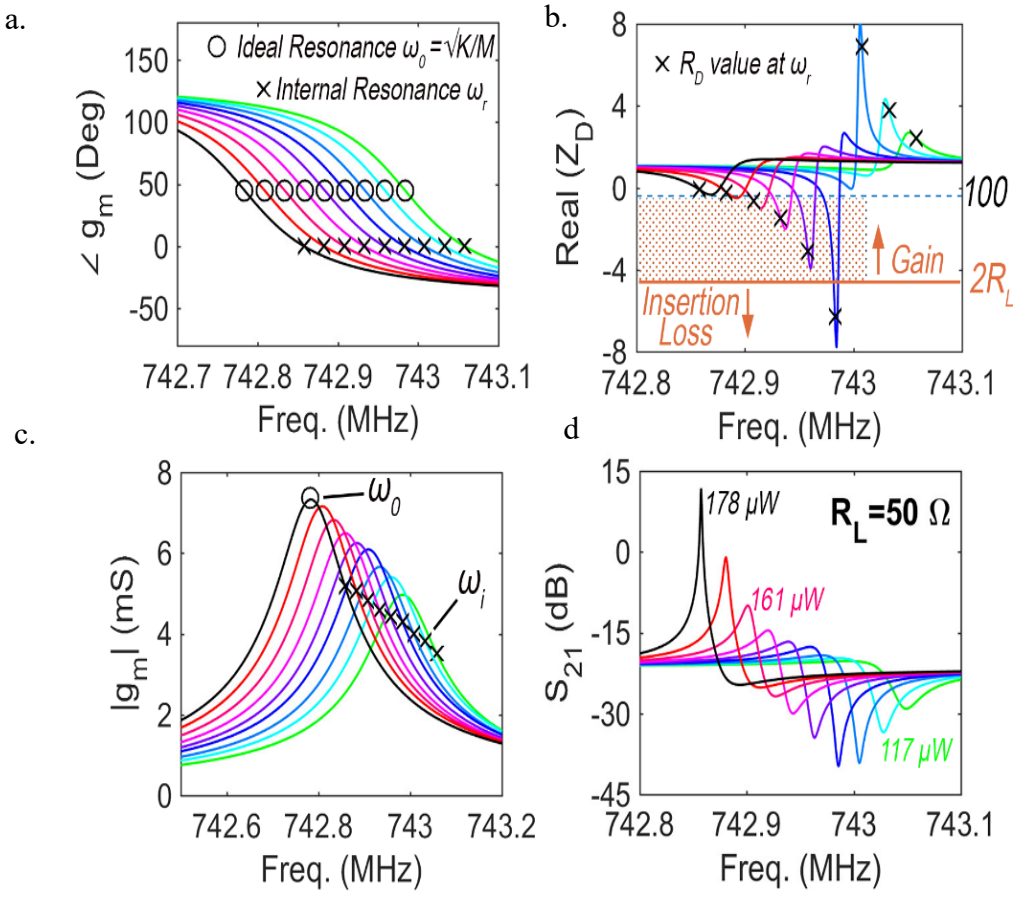


Figure 3.15. Numerical calculations based on the frequency dependent model using the FEA results. Real part of the device impedance marks the overall resistance of the device at resonance and the active region where gain is possible.

To validate the model, two devices with similar 200nm × 50nm piezoresistive nanobeams are fabricated on a silicon on insulator (SOI) substrate with a 300nm thick silicon device layer and a 400nm thick buffer oxide. Square-shaped masses with dimensions of 1.5µm and 800nm are chosen to lead to operating frequencies of approximately 400 and 750MHz. In order to reach such small dimensions, electron beam lithography (EBL) was used to pattern a 240nm thick poly (methyl methacrylate) (PMMA) e-beam resist (Figure 3.16b).

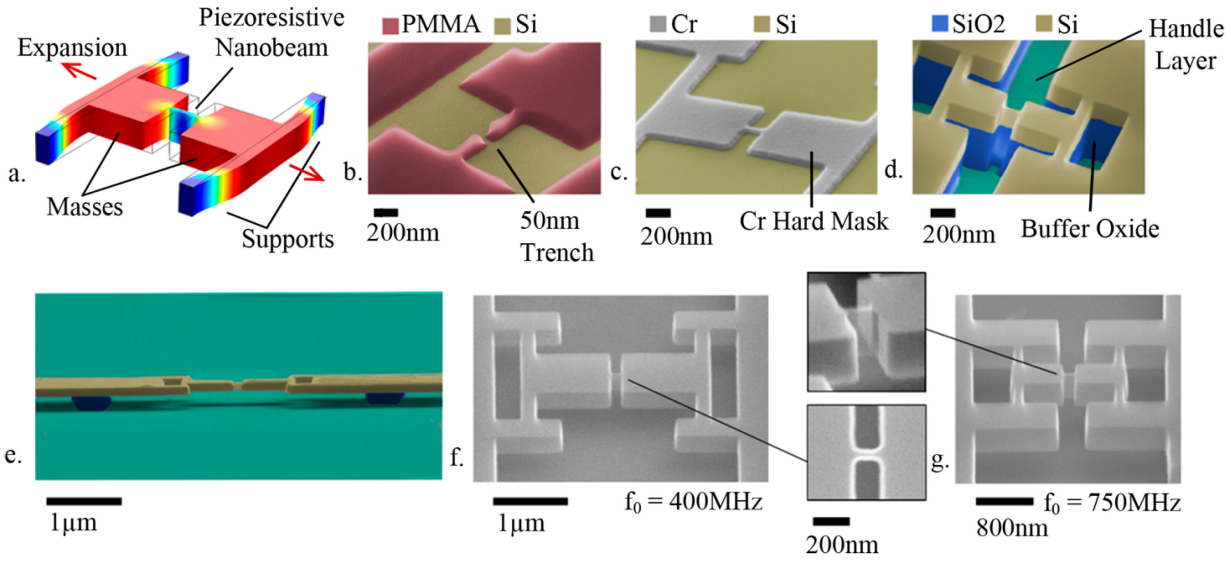


Figure 3.16. (a) Schematic view showing the structure and in-plane resonant mode shape of a nanomechanical piezoresistive amplifier. (b) The patterned device shape including a 50nm wide trench on PMMA using EBL at 20KeV. (c) The Cr hard mask after the lift-off process. (d) Etching the device pattern onto the Si device layer and buffer oxide layer using chlorine-based plasma. (e) Released structure after HF dip. (f, g) Different views of the completed devices with operating frequency of 400 and 750MHz.

A 50nm layer of Cr was then evaporated on to the sample to form a hard mask via lift-off (Figure 3.16c). This was followed by chlorine-based inductively coupled plasma etching of the device patterns onto the Si device layer (Figure 3.16d). Finally, to suspend the devices the substrate is exposed to 49% hydrofluoric acid, where the buffer oxide layer underneath the patterned silicon

(Figure 3.16e) is removed. Figure 3.16f, g show scanning electron micrographs of the fabricated devices.

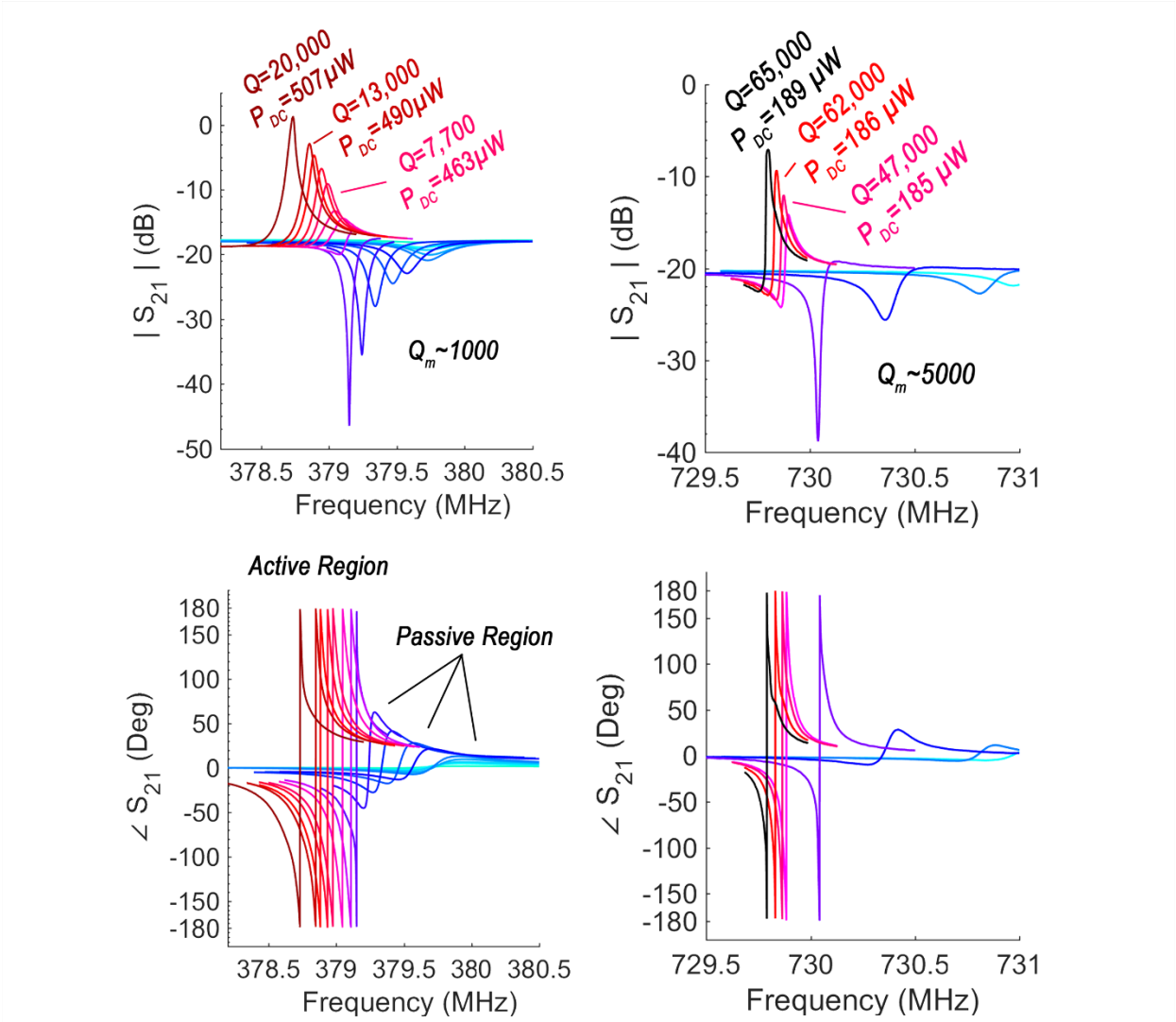


Figure 3.17. The measured $S_{21}$ response of the fabricated devices that include the loading effects of the parasitic elements as well as the 50Ω termination of the network analyzer showing minimal insertion loss with large quality factors.

Figure 3.17 shows direct measurements of the fabricated devices taken from a network analyzer without any parasitic cancellation (i.e., they include the loading effect of the wire-bond pad capacitances and the 50Ω terminations of the network analyzer). It is crucial to notice the very

low insertion loss of 6dB with a large $Q$ for such small device at UHF, even in the presence of significantly large parasitic elements. $g_m$ values extracted from the measurements, as shown in Figure 3.18 are in strong agreement with the theoretical predictions in Figure 3.15 ($g_m$ value of 4 mA/V for 189 μW).

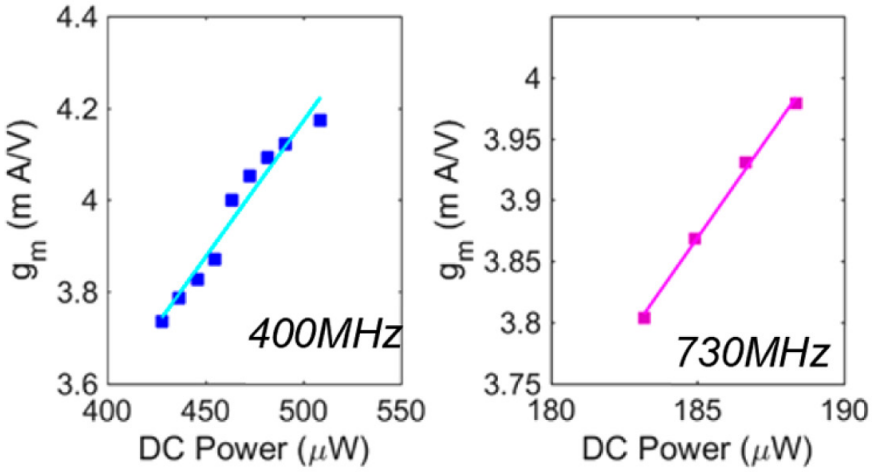


Figure 3.18. The measured motional transconductance as a function of dc power showing close agreement to the numerical calculation

Figure 3.19 shows the projected $S_{21}$ response of the fabricated device after elimination of parasitic elements on a 50Ω, 150Ω and 250Ω loads. By matching the device to larger values of load (i.e., RL > 50 Ω), larger effective quality factor and signal transmission at resonance can be achieved for a smaller gm and dc power (e.g., 10dB gain, Q of 330,000 for a 250Ω load). However, the $g_m$ values that can satisfy the gain condition (i.e., $R_L < |R_D| < 2R_L$) can now be obtained in a smaller range of DC currents (lower downward peaks in Figure 3.15 b). Also, as discussed, at very large loads ($R_L \gg R_A$) the device is ultimately loaded by its own physical resistance $R_A$ and can be pushed to an unstable region (i.e., self-sustained oscillation) if $|1/g_m| < R_A$. Therefore, as long as the stability condition is satisfied, the maximum attainable quality factor is limited by the

smallest matching range the load can provide as well as the fluctuations in DC power that can change the value of device resistance $R_D$.

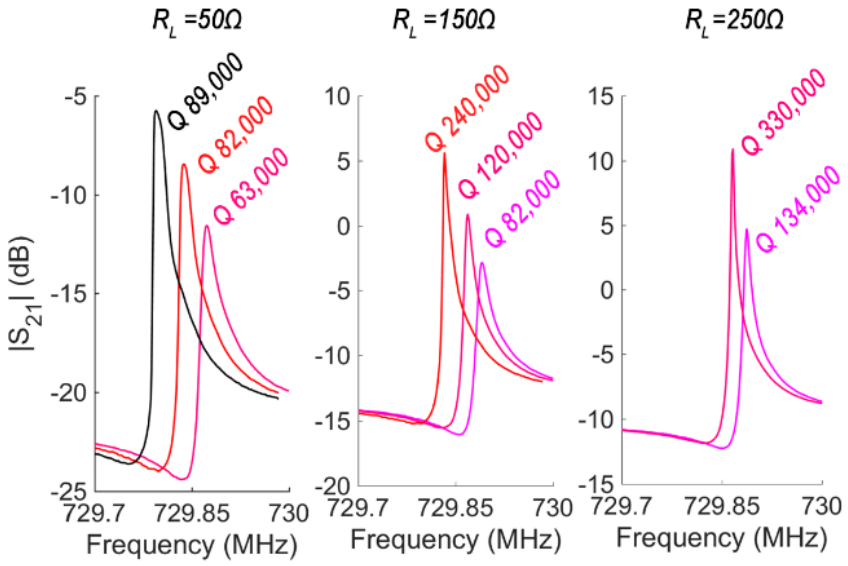


Figure 3.19. The measured $S_{21}$ frequency responses of the fabricated devices with loads of 50,150 and 250Ω

### 3.3.2 Figure of merit

Further downscaling of the nanobeam will lead to a stronger internal amplification while the device consumes similar power at higher frequencies. The strength of the internal amplification, that is, the voltage gain induced across the piezoresistor by the motional current $i_m$, is determined by the product of $g_m$ and $R_A$, referred to as loop gain. Assuming the mechanical frequency is kept much larger than thermal cut-off frequency so that the temperature response is inversely proportional to the thermal capacity of the beam:

$$\frac{V_{ac,m}}{V_{ac,in}} = \frac{i_m . R_A}{v_{ac}} = g_m R_A \propto \alpha . \pi_l . Q_m . V^{-1} f^{-1} . P_{DC} \tag{3.7}$$

where $V_{ac,in}$ is the initial ac voltage across the beam, $V_{ac,m}$ is the voltage induced by the motional current and $\alpha$, $\pi_l$, $Q_m$, $V$, and $f$ are the thermal expansion coefficient, piezoresistive coefficient, mechanical quality factor, beam volume, and operating frequency. As shown in Figure 3.20, because the two devices have similar beam dimensions with mechanical quality factors of 1000 and 5000 at 400 and 730 MHz, respectively, the two devices show similar loop-gains.

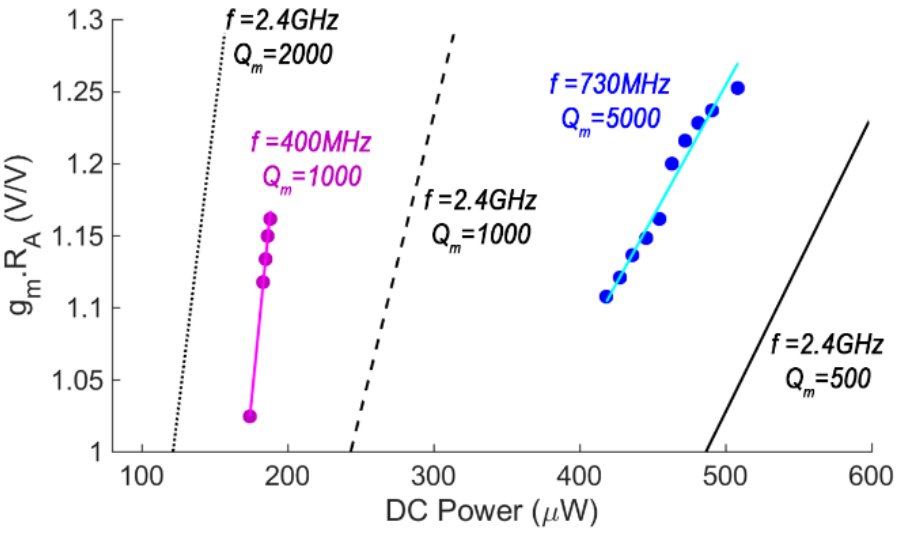


Figure 3.20. Loop gain, a measure of internal amplification strength plotted vs. DC power consumption for measured devices as well as possible loop gains for a 2.4GHz device. Assuming same material parameters (e.g., $\pi_l$, $\alpha$, E), the 2.4GHz device shows similar loop gains for a reasonable range of power consumption even with a lower mechanical quality factor.

To achieve the same level of loop-gain at higher frequencies under the same mechanical quality factor, the beam dimensions must be reduced. Assuming similar parameters (e.g., $\alpha$, $\pi_l$, etc.), a device fabricated on a 150nm device layer with 30 nm × 100 nm beam dimensions and 0.09 $\mu m^2$ mass area can potentially deliver a similar loop-gain at 2.4 GHz (for GSM and CDMA standards). It is hard to precisely predict mechanical quality factor of such device; therefore, the loop-gains

are plotted for mechanical quality factors of 500, 1000, and 2000 to predict the hypothetical required dc power consumption at such frequency.

### 3.3.3 Comparison to state-of-the-art

It was shown that as predicted by the theory, nanomechanical piezoresistive amplifiers can offer sharp filtering characteristics along with active signal amplification in the UHF range.

Table 3.3. Comparison of the state of the art microscale UHF electromechanical resonant devices demonstrating the fact that while capacitive and piezoelectric devices share a trade-off between quality factor and insertion loss, the nanomechanical piezoresistive amplifier can achieve unprecedented values for both.

| Device Type | Material | Area Size ($um^2$) | Frequency | Quality Factor | $P_{DC}$ ($\mu W$) | $S_{21}$ (dB) $R_L$=50Ω | Reference No. |
|---|---|---|---|---|---|---|---|
| Capacitive | Diamond | 870 | 800MHz | 77,000 | Passive | -54 | [15] |
| Piezoelectric | Lithium Niobate | 12,800 | 750MHz | 300 | Passive | -4 | [16] |
| Capacitive/ Piezoelectric | Aluminum Nitride | 2,800 | 1.2GHz | 3,000 | Passive | -20 | [20] |
| Piezoelectric/ HEMT | AlGaN/GaN | 25,000 | 900MHz | 8,350 | <100 | -60 | [24] |
| Piezoelectric/ HEMT | AlGaN/GaN | 14,000 | 512MHz | 13,000 | <100 | -20 | [23] |
| Piezoresistive | Si | 50 | 30MHz | 260,000 | 1000 | - | This Work |
| Piezoresistive | Si | 1.4 | 730MHz | 89,000 | 189 | -5 | This Work |

Having dimensions in the nanoscale is crucial for such devices to reach acceptable performance, a trait that most electromechanical devices do not share. Table 3.3 shows a comparison of the

presented device with other state of the art miniaturized electromechanical UHF resonator technologies.

### 3.4 Discussions and Future Work

Frequency tuning range and noise performance of the nanomechanical amplifiers require further study. Tuning of the resonance frequency to cover a wider range of frequencies can be accomplished by controlling the dc bias current. As shown in Figure 3.17, at high gains a slight change in the dc current can tune the resonance frequency due to the temperature dependence of Young's Modulus. However, changing the dc current may result in a significant loss of gain under a constant load, and the load must be adjusted accordingly to compensate (a similar gain can be achieved for a smaller gm but a larger load). The tuning range will be limited to the dc current range that can yield a negative $R_D$ and tunability of the load ($R_L$). Another significant aspect is the noise analysis of such narrowband amplifiers. There are two major sources of noise that could impact the device, the thermal noise of the physical resistance $R_A$ and Brownian noise imposed on the vibrating masses in the air. Whereas the latter can be suppressed when operating inside the vacuum, the former is expected to be dominant. Therefore, the noise behavior of the nanomechanical amplifier is expected to be similar to that of a solid-state transistor of the same size. Further, the narrowband filtering can suppress most components of the white noise by amplifying an ultranarrow bandwidth. Although in the model presented in this work three separate systems/transfer-functions are used to describe the signal transmission, the entire internal amplification process happens in one element (the piezoresistor) simultaneously. Therefore, this electrical model may not adequately represent the noise behavior of the devices. Complete noise

parameter measurements under various loads can provide a comprehensive understanding of the noise behavior and develop an accurate noise model.

Power handling is another subject that requires further investigation. Once the dimensions are aggressively scaled down, the device will have a very limited power handling and will reach its linear operation range at low input AC powers. One possible solution to address such issue is to use mechanically coupled arrays of the devices so that a large number of electrically parallel nano-beam piezoresistors are embedded in the device structure between side-coupled resonant masses. In this manner, the DC bias power, as well as the input AC power, will be distributed among identical piezoresistors in the entire array. Dividing the DC bias power among different parallel piezoresistors, however, has a negative effect on the overall achievable loop gain (while maintaining the same power consumption). The loop gain is proportional to the square of the bias current and the physical resistance of each nano-beam. By placing multiple piezoresistors in parallel, the bias current will be divided between them and the resistivity of the structural material, and therefore the physical resistance of each nano-beam is to be increased by the number of paralleled nano-beams to maintain the same power consumption. As a result, the overall loop gain drops by the number of paralleled beams and to maintain the same loop gain (the same overall motional negative resistance), the nano-beam dimensions need to be further shrunk down.

Finally, even though silicon was used as the piezoresistive material in this study, the design of the proposed nanoelectromechanical narrow-band amplifier is not limited to silicon. The proliferation over the past few years of novel materials such as wide-bandgap semiconductors, including GaN and SiC, and their growing applications in RF/power electronics as well as M/NEMS, suggests that they can create exciting opportunities and potentially replace silicon in

many areas, including in the design of the device proposed in this study. They can also offer electrical and mechanical properties that match and even exceed those of silicon. Greater thermal and mechanical stability at temperatures as high as 600 °C, piezoresistive coefficients comparable to that of silicon, and higher Young's moduli [31], [50]–[53] make these materials suitable alternatives for silicon as the basis of the nanoelectromechanical amplifier, particularly in harsh environments where silicon fails to retain its properties.

# CHAPTER 4

# SIDE PROJECTS

## 4.1 Piezoelectric Micro-Resonators for High-Resolution Gas Flowmetry[1]

This work presents sail-shaped thin film aluminum nitride resonators operating as high-resolution gas flow meters. Deformation of the sail-like structure of the resonator due to the gas flow changes the effective stiffness and consequently the resonant frequency of the resonator. For a 10.2 MHz resonator engaged in a simple oscillator configuration Allan deviation as small as *10-8* (*df/f0*) was achieved for measurement periods less than one minute. The sensitivity of frequency to flow velocity was measured to be 0.5Hz/mm/s leading to the minimum detectable velocity of 0.2mm/s. In addition, the transient behavior of the sensor was investigated showing a rise time of approximately 20 ms. The presented sensors with frequency modulated output are much less susceptible to noise compared to the conventional sensors with amplitude modulated output. Furthermore, the output of such sensors can be directly fed into a digital readout/control system without the need for analog to digital conversion.

Flow sensors are among the most widely used sensors due to their applications in various industrial and scientific areas including bioanalysis, metrology, civil engineering, the transport and process industry, environmental sciences, medical technologies, and climate control [54]–[58].

---

[1] © 2015 IEEE. Reprinted, with permission, from Ramezany, A., M. Mahdavi, A. Moses, and S. Pourkamali. "Sail-shaped piezoelectric micro-resonators for high resolution gas flowmetry." In *Solid-State Sensors, Actuators and Microsystems (TRANSDUCERS), 2015 Transducers-2015 18th International Conference on*, pp. 2252-2255. IEEE, 2015.

The most common categories of flow sensors operate based on heat transfer through the gas flow and temperature drift of certain material properties (e.g. electrical resistance). Generally, thermal flow sensors measure the effect of the flowing fluid on the temperature of a hot body while maintaining constant heating power, or by detecting the asymmetry of temperature profile around the heater [59]. However, when dealing with a mixture of gases or unknown levels of moisture, such devices lack accuracy due to possible fluctuations in thermal properties of the gas.

Optical flow sensors, on the other hand, are safer around volatile gases, have greater durability at elevated temperatures and are corrosion resistant. Nevertheless, their biggest disadvantages are their large size, relatively high cost and complex setup [60].

MEMS-based flow sensors can offer a compact, low cost and accurate solution to the problem of gas flow measurement. MEMS flow sensors can be also classified as thermal or non-thermal based on their mode of operation [60]. If sensitive enough, non-thermal MEMS flow sensors have the potential to replace thermal based flow sensors in some applications especially when a mixture of gases or unknown levels contaminants are present.

Most popular non-thermal MEMS flow sensors operate based on force transfer mechanisms, in which a drag, lift, or Coriolis force is exerted upon the device body by the flow. A capacitive or piezoresistive transducer then translates the mechanical force into an electrical output [61]–[63]. Almost all existing flow sensors provide analog amplitude modulated outputs that can be easily disturbed by electronic noise or environmental interferences and require analog to digital conversion to interface with the dominantly digital state of the art electronics.

The flow sensor demonstrated in this work can address the limitations of thermal detection utilizing the sensitivity of a bulk mode resonant sail-shaped structure to the perpendicular flow drag force. In addition, its frequency modulated output offers significantly improved noise and interference robustness and can be directly fed into a digital counter without the need for an analog front-end for signal conditioning and analog to digital conversion.

Figure 4.1 shows the SEM image of the piezoelectric micro-resonator used in this work consisting of a 1μm thick AlN sandwiched between a 150nm thick layer of Molybdenum as the bottom electrode and a 100nm layer of platinum as the top electrode. The device is designed to operate in its 2nd lateral extensional resonance mode where the two sections of the resonator beneath the electrically isolated top metal electrodes undergo out of phase lateral expansion and compression.

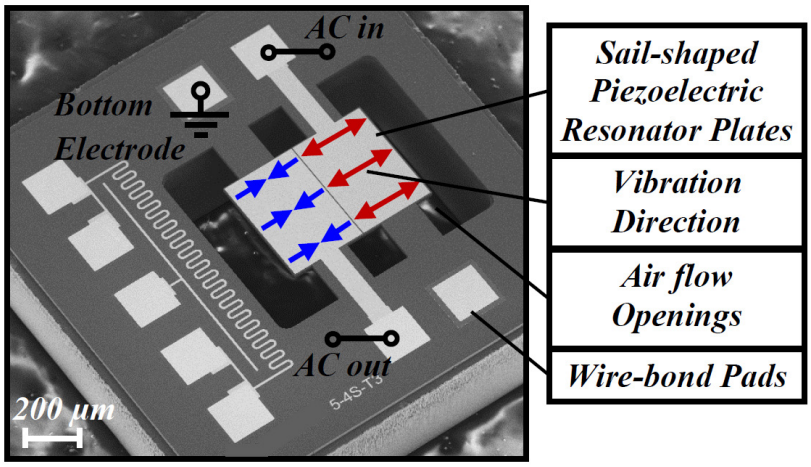


Figure 4.1. SEM view of the AlN resonator with Sail-Shaped structure designed to operate in its second lateral extensional mode.

Figure 4.2b shows the deformation of the resonating body created by a uniform perpendicular force.

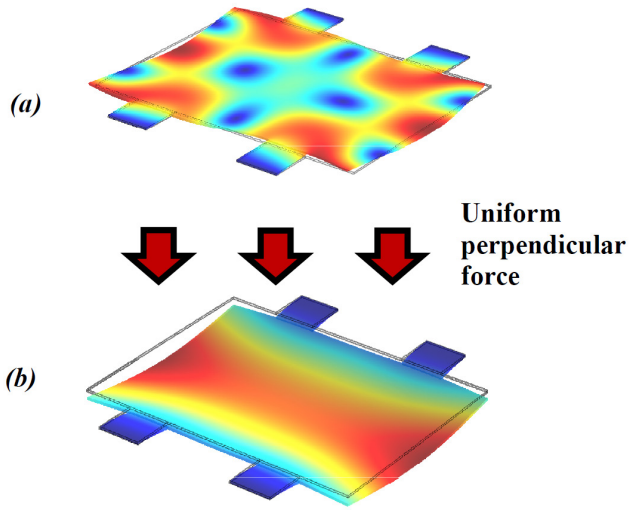


Figure 4.2. COMSOL simulation for the 2nd lateral extensional mode of the AlN resonator (a) with no external force and (b) in the presence of a uniform perpendicular force. The displacements are exaggerated for demonstration

As depicted by the frequency response obtained from the network analyzer Figure 4.3, the piezoelectric microresonator operates at around 10.2 MHz with the quality factor of 700 in the air. A highly stable electronic oscillator operating at the same frequency can be realized by interfacing the resonator with a simple CMOS inverter acting as the sustaining amplifier. The perpendicular force from the gas flow imposed upon the relatively large (630μm×~520μm) and thin (~1.2μm) sail-shaped resonator body can change the relative stiffness and consequently the oscillator frequency.

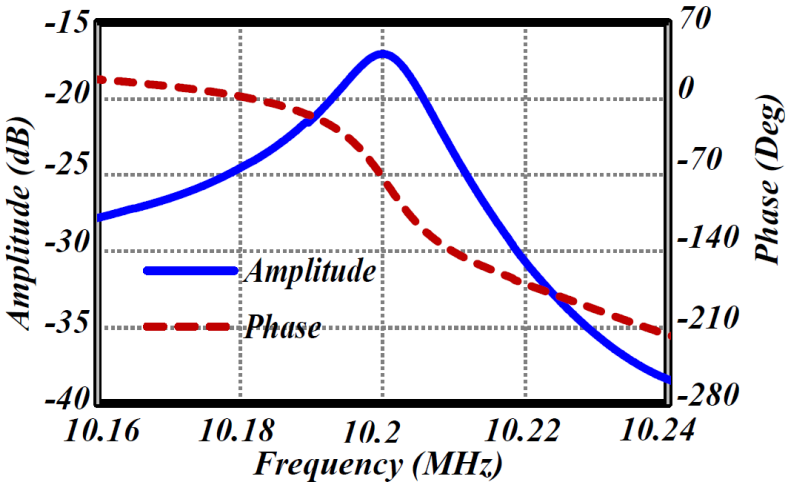


Figure 4.3. Measured frequency response for the 2nd lateral extensional mode of the resonator showing a resonant frequency of 10.2 MHz and quality factor of 700.

Fabrication of the sail-shaped piezoelectric resonator starts with the deposition of a 150nm thick layer of Molybdenum followed by 1µm of Aluminum Nitride, on an SOI substrate (Figure 4.4a). AlN is then patterned in order to gain access to the bottom electrode, i.e. the Mo layer, followed by deposition and patterning a 100nm layer of Platinum as the top electrode as shown in Figure 4.4b. The wire bond pads are then covered with gold, and a 2µm thick LPCVD oxide is used as the hard mask to pattern the device (Figure 4.4c.). AlN and the silicon device layer are then etched by a chlorine-based plasma and Bosch process (DRIE) respectively, as shown in Figure 4.4d. Eventually, the silicon handle layer and the buffer oxide layer are etched from the backside to suspend the structure and form a path for the gas flow through the chip. In addition, to reduce the stiffness and, therefore maximize the sensitivity of the sail-shaped resonator to perpendicular forces, the silicon device layer is also removed from the backside of the AlN-metal sandwich. The completed structure is shown in Figure 4.4e.

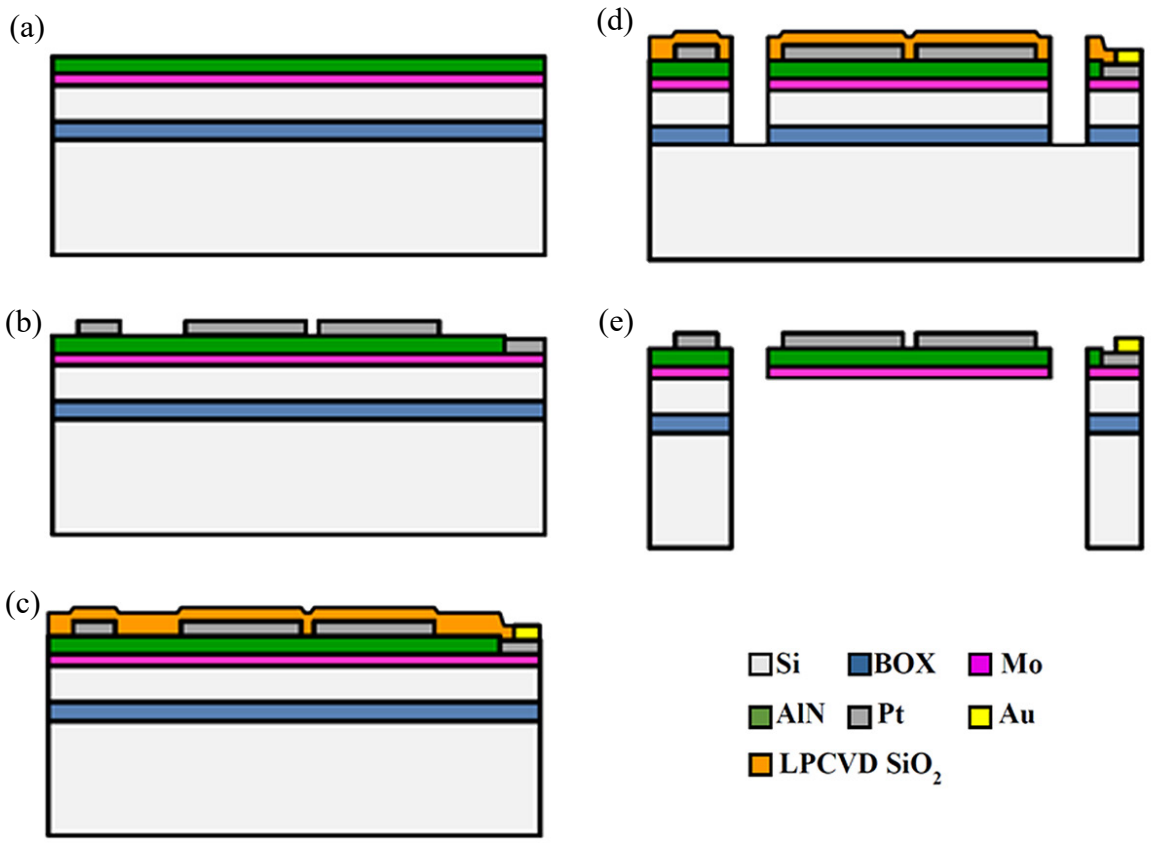


Figure 4.4. Fabrication process for sail-shaped piezoelectric micro-resonator. (a) Deposition of Mo and AlN on 100 SOI wafer. (b) Deposition and patterning of Platinum layer as the top electrode. (c) LPCVD oxide used as the hard mask and covering the wire-bond pads with gold. (d) Etching the AlN and the silicon device layer using ICP and DRIE. (e) Removing the handle layer and the Box layer from the backside.

A fabricated device was mounted on a PCB containing a CMOS inverter as the sustaining amplifier and a few capacitors and resistors for biasing, decoupling, and phase shift tuning to form an electronic oscillator utilizing the resonator as its frequency reference.

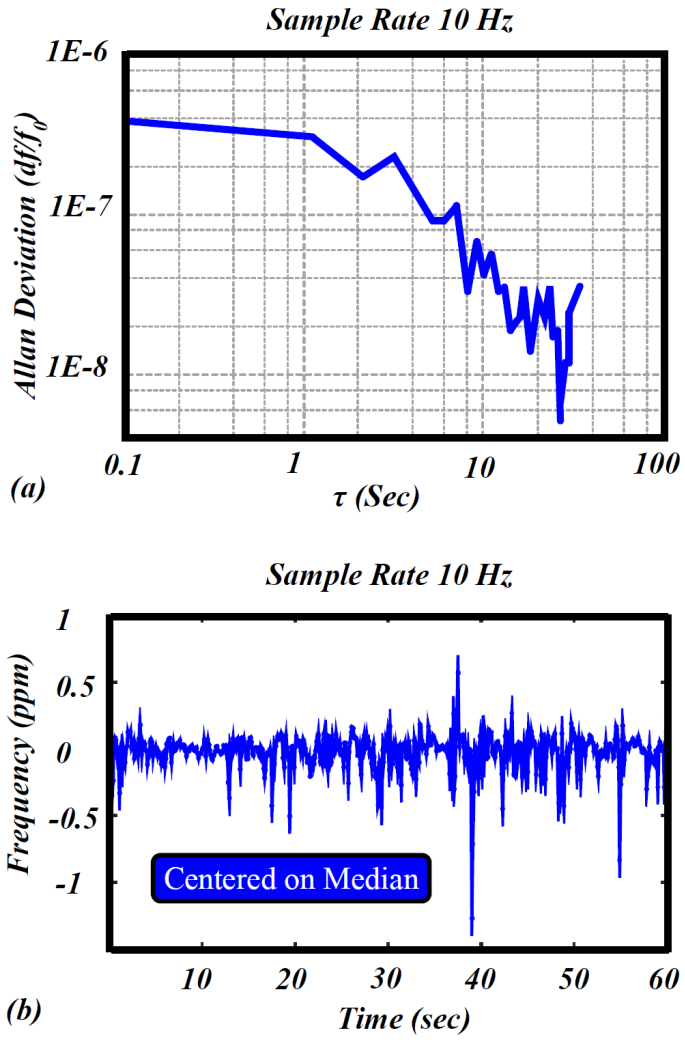


Figure 4.5. (a) Measured Allan deviation for the oscillator utilizing the MEMS resonator as its frequency reference measured with a sample rate of 10Hz indicating the noise floor of 10-8 can be achieved in less than one minute. (b) Frequency fluctuations of the oscillator measured with sample rate of 10Hz.

The stability of the oscillator output frequency sets the limit on the minimum detectable frequency shift and therefore the gas flow measurement resolution. Figure 4.5a shows the measured Allan deviation of the resulting oscillator showing the noise floor value of *df/f0=10-8*, associated with a 0.1Hz shift in frequency that can be achieved in less than one minute. The

minimum Allan deviation value can also be interpreted as the minimum frequency shift that is potentially measurable. Figure 4.5b shows 600 measured oscillation frequency data points centered on the median value during the measurement of Allan deviation.

To measure the response to air flows, a sealed flow chamber was mounted on top of the PCB containing the piezoelectric oscillator, as shown in Figure 4.6. The flow outlet is directly located below the device to maximize the perpendicular force imposed on the sail-shaped resonator plate. Furthermore, to keep the flow chamber from pressurizing, the flow inlet and outlet are chosen to have the similar diameters.

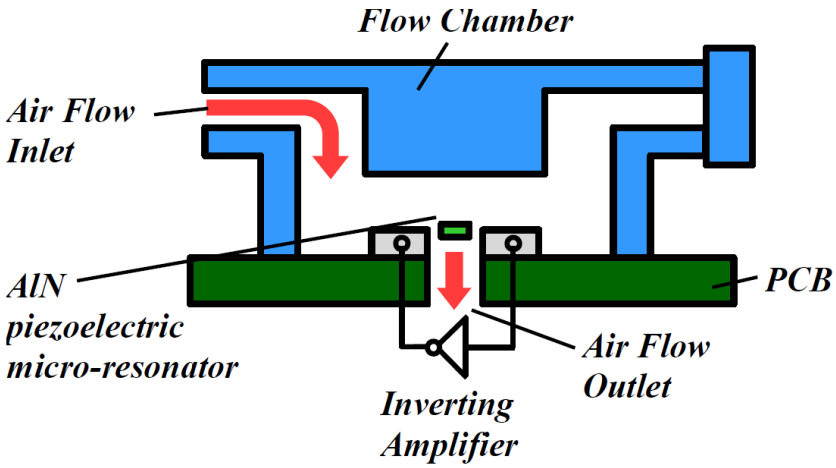


Figure 4.6. Cross sectional view of the flow chamber.

Air flows regulated by a manual flowmeter were directed towards the chamber, while changes in the oscillation frequency were measured and recorded using the microprocessor-based characterization board, essentially the frequency counter, depicted in Figure 4.7. Figure 4.8 shows the measured output frequency shift in response to airflow velocity. The extrapolation of the measured data indicates that the frequency of oscillation follows the trend estimated by Equation 4.1, where $\Delta f$ is the output frequency change, and $V$ is the flow velocity. According to Equation

4.1 the potential minimum detectable frequency of 0.1Hz requires a flow velocity of approximately 0.2 mm/s.

$$\Delta f \approx 480 \times V \tag{4.1}$$

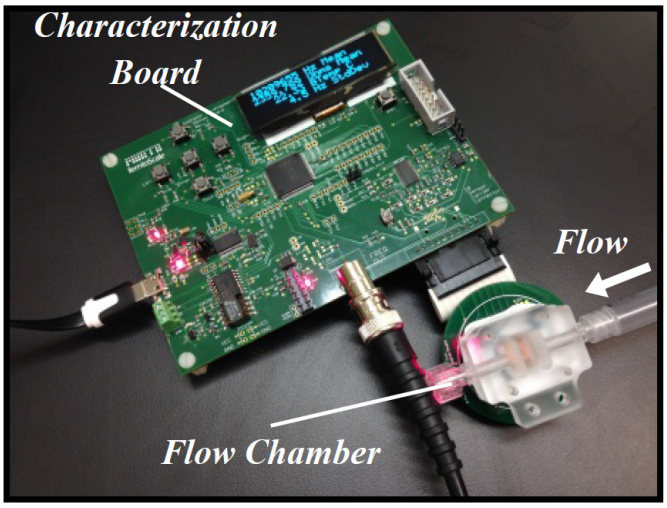


Figure 4.7. The measurement setup including the characterization board and flow chamber.

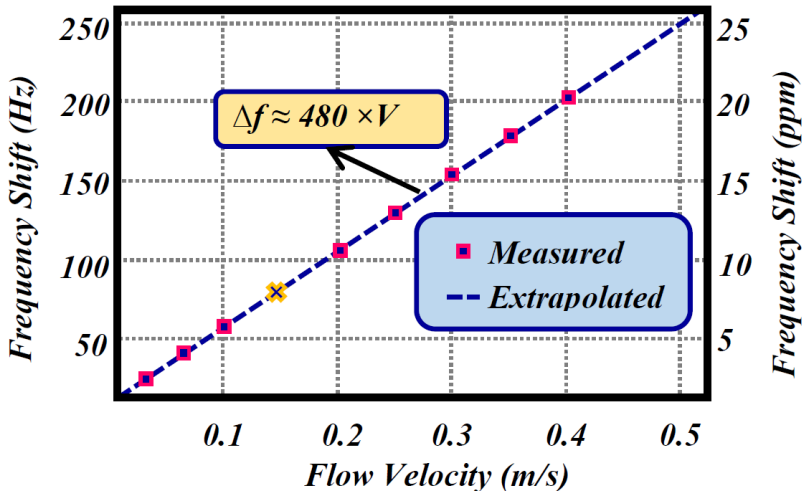


Figure 4.8. Oscillator frequency shift as a function of air flow velocity.

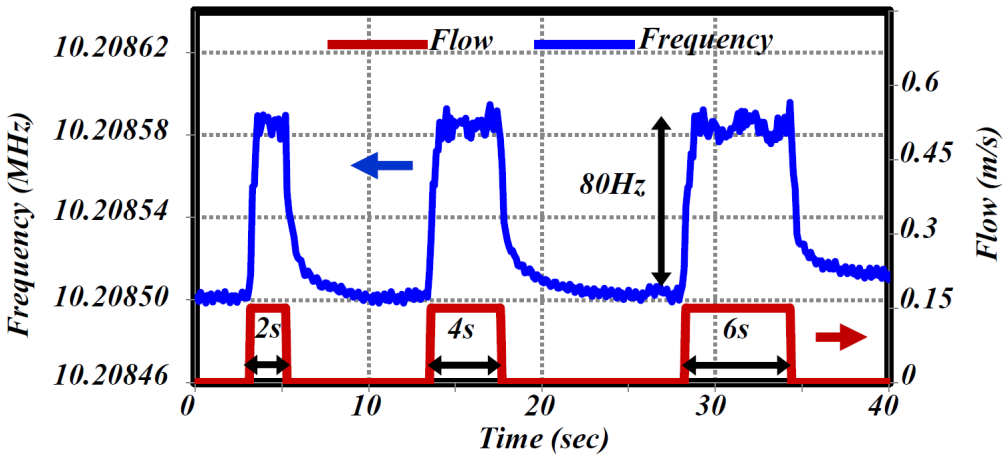


Figure 4.9. Time response of the oscillator to a fixed flow with the velocity of 0.15 m/s applied intermittently for durations of 2, 4 and 6 seconds. Frequency shift of 80Hz in accordance with Equation 4.1 was achieved regardless of the duration of the flow. Rise and fall time of approximately 20ms was measured with the sample rate of 1 kHz.

In order to characterize the time response of the microresonator to air flows, a fixed flow of 0.15m/s velocity was intermittently applied for durations of 2, 4 and 6 seconds. As shown in Figure 4.9 such flow velocity leads to a steady state frequency shift of 80Hz that matches the results shown in Figure 4.8 (denoted with a yellow cross). According to the measurements with a sample rate of 1 kHz, the device is capable of responding to the flow with a rise time of ~20ms.

## 4.2 Frequency Modulated Electrostatically coupled Resonators for Sensing Applications[2]

This work presents a proof-of-concept for a frequency modulated output MEMS sensor based on the electrostatic coupling of two resonators. Change in the gap between a single resonator

[2] © 2016 IEEE. Reprinted, with permission, from Ramezany, Alireza, Vahid Qaradaghi, Varun Kumar, and Siavash Pourkamali. "Frequency modulated electrostatically coupled resonators for sensing applications." In *SENSORS, 2016 IEEE*, pp. 1-3. IEEE, 2016.

and a movable capacitive electrode can modulate the electrostatic force acting on the resonator, and therefore, alter its resonance frequency. A second resonator is used as the movable electrode to facilitate displacement amplification in response to the external force at resonance. In this work, clamped-clamped beams are used for both resonators. Three devices are fabricated with different dimensions, and a DC magnetic field is used to actuate the second beam at the resonance frequency, while the frequency of the first beam is monitored. It is shown that by actuating the movable electrode at its resonance, sensitivity is enhanced by more than 3 orders of magnitude compared to DC actuation, and sensitivity of 8Hz/mAmT is achieved for a device with 1000μm×5 μm and 200μm×3μm beams and a capacitive gap of 1.5μm. While Lorentz force is used to actuate the beam in this work, the concept is not limited to magnetic field sensing.

For more than a decade, resonant MEMS sensors have offered a promising solution to the problem of force measurement. Resonant MEMS accelerometers [64], and magnetic sensors [65], [66] are a few examples of such efforts. Indirect modulation of the resonance frequency of a resonator in response to an external force, in contrast, to directly affecting its mechanical stiffness or mass has proven to provide higher sensitivity. In [67], for example, a perturbation in the system of two identical electrostatically coupled resonant beams affects the amplitude ratio of the two resonance modes by orders of magnitude more than it would affect each resonant beam individually.

Even though extensive research has been performed on electrostatically coupled sensors with amplitude modulated outputs [68]–[70], the use of electrostatic modulation on frequency has not been fully investigated. In principle, a change in the electrostatic force acting on a resonator in

response to an external stimulus can modulate its resonance frequency. This principle has been previously demonstrated to realize wideband MEMS filters [71]. In this paper, we propose to use electrostatic modulation of a resonator for sensing applications. An external force (e.g. a force created by a magnetic field, acceleration, or pressure) can move a capacitive electrode away or towards the resonator and modulate its frequency. It is shown that if the movable electrode is also actuated at its resonance, sensitivity can be improved by orders of magnitude.

As it has been previously demonstrated in [72], the resonant frequency of a capacitively actuated clamped-clamped beam can be tuned by modulating the electrostatic forces acting on the beam. In essence, the electrostatic forces in the capacitive actuation and read-out act as negative springs coupled to the resonant beam. Equation 4.2 shows the resonance frequency of a resonator with mechanical stiffness and mass of $K_r$ and $M_r$ that is coupled to a capacitor on each side [9].

$$f = f_0 \sqrt{1 - \frac{V_{B1}^2 C_{Aeff}}{K_r {g_A}^2} - \frac{V_{B2}^2 C_{seff}}{K_r {g_s}^2}} \tag{4.2}$$

$f_m$ is the mechanical resonant frequency of the resonator before tuning, $g_A$, $C_{Aeff}$, $V_{B1}$, the actuating gap, effective capacitance, and voltage across the actuating capacitor, respectively. $C_{seff}$, $g_s$, $V_{B2}$ are similar parameters of the sensing capacitor. According to this equation, any change in bias voltages or capacitive gaps can modulate the resonant frequency. A capacitively coupled micromechanical actuator (e.g. a clamped-clamped modulator beam) can modulate the gap and therefore, the resonant frequency. Equation 4.3 shows the sensitivity of such a system to an external force $F_{ext}$.

$$\left.\frac{df}{dg_s}\right/_{F_{ext}} = \frac{3f_m \frac{V_{B2}^2 \epsilon_0 t L_s}{K_r {g_s}^4}}{\sqrt{1 - \frac{V_{B1}^2 \epsilon_0 t L_A}{K_A {g_A}^3} - \frac{V_{B2}^2 \epsilon_0 t L_s}{K_r {g_s}^3}}} \cdot \frac{1}{K_{beff}} \tag{4.3}$$

where $K_{beff}$ is the effective stiffness of the modulator beam. Figure 4.10 depicts the schematic of a clamped-clamped resonator beam capacitively coupled to a clamped-clamped modulator beam. In the presence of a magnetic field, a DC current $I_L$ passing through the modulator beam can modulate the sensing gap and the resonance frequency by moving the modulator beam towards or away from the resonator.

The sensitivity of such magnetic sensor can be improved significantly if the modulator beam is also actuated at its resonance frequency. At resonance, the modulator beam can change the gap $Q$ (quality factor) times more compared to when it is actuated with a DC force with the same amplitude. However, when both beams are resonating, each can affect the other. Ideally, the modulator beam is required to modulate the frequency of the resonator beam without being affected by its electrostatic modulation. In addition, according to Equation 4.3, the softer the resonator beam, the more sensitive it is to changes in the gap. Therefore, the resonator beam must have a lower stiffness than the modulator beam. On the other hand, a soft modulator beam is desirable to change the gap in response to small external forces. According to Equation 4.3, reducing the sensing gap $g_s$ can significantly improve the sensitivity. Even though reducing $g_s$ limits the pull-in voltage, its contribution to sensitivity outweighs the reduction in the bias voltage $V_{B2}$.

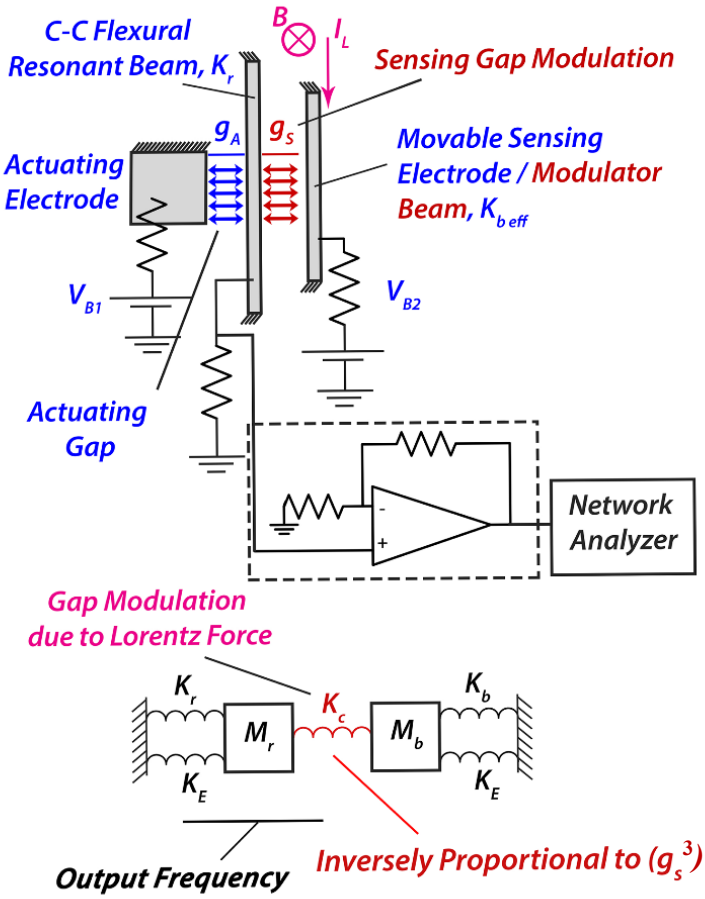


Figure 4.10. Schematic view of two capacitively clamped-clamped beams. As the modulator beam on the right moves towards or away from the resonant beam, the coupling stiffness $K_C$ is modulated and affects the resonance frequency of the resonant beam.

To find the optimum design, three devices with different dimensions are fabricated on an SOI wafer with 15μm device layer with 0.03 Ω.cm resistivity. Dimensions of the devices are shown in Table 4.1. As shown in Figure 4.11, the SEM view of device #2, a 1000μm long resonator beam and a 200μm long modulator beam are separated by a 1.5μm gap (limited by optical lithography).

Table 4.1. Device dimensions

| $g_A$= 3µm | $g_S$= 1.5µm | Device #1 | Device #2 | Device #3 |
|---|---|---|---|---|
| Resonator Beam | Length (µm) | 750 | 1000 | 1000 |
| | Width (µm) | 6 | 6 | 5 |
| Modulator Beam | Length (µm) | 200 | 200 | 200 |
| | Width (µm) | 6 | 6 | 3 |

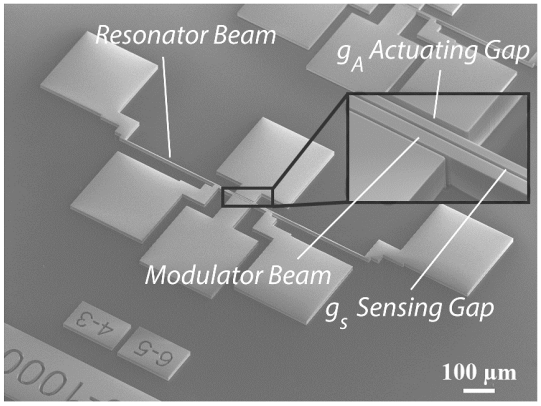


Figure 4.11. SEM view of Device #2

As stated before, the resonator beam is chosen to be shorter than the modulator beam to both increase the sensitivity to gap change and reduce the modulation of the modulator beam itself. As shown in Figure 4.10, the resonator beam is connected to a network analyzer through an amplifier to prevent loading of the large motional resistance of the resonator by 50Ω port of the NA. For DC measurements, a variable DC current is passed through the modulator beam while the resonance peak of the long beam is monitored. For every current, before and after applying a magnetic field of 30mT, the resonance frequencies are compared to eliminate the effect of electrostatic tuning by DC bias voltages. For AC measurements, under the same bias voltages similar experiments are performed, except instead of a DC current, an AC current is passed through the short beam. While

the resonance frequency of the long beam is monitored, the frequency of the actuating current is swept in the proximity of resonance frequency of the short beam. It is observed that as the frequency of the actuating current approaches the resonance frequency of the modulator beam, the shift in the long beam continually increases.

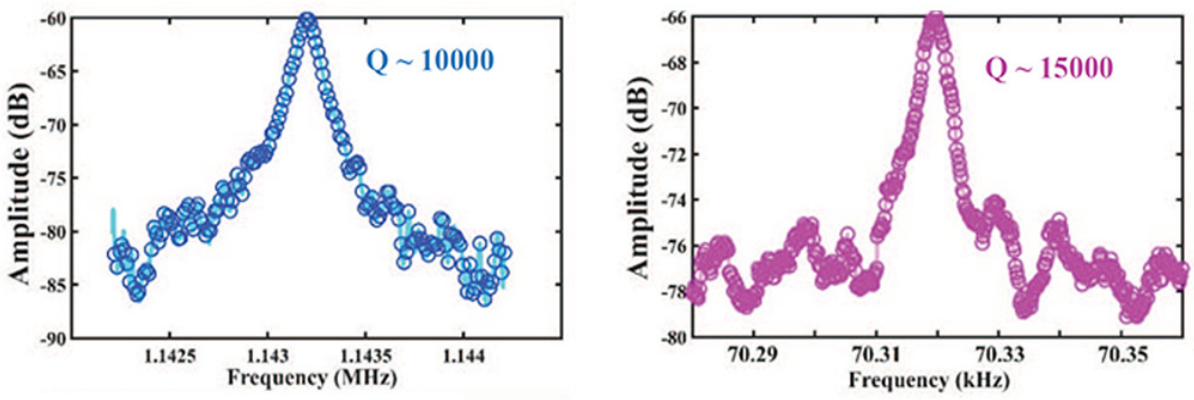


Figure 4.12. Measured frequency response of each beam for Device #2.

Figure 4.12 shows the frequency responses of the beams for device #1. The AC measurement results are shown in Figure 4.13 for all three devices. The frequency shift of the long beams is measured in response to various AC currents for multiple bias voltages under a magnetic field of less than 30mT. Sensitivity is measured to be 8 Hz/mAmT, and considering standard deviation of 50mHz (measured for 300 seconds in 1-second intervals) as the minimum detectable shift, the minimum detectable field of 6μT/mA is achieved.

To observe the enhancement in sensitivity from DC to AC actuation, an enhancement factor E.F is defined as the ratio of the sensitivity of a device actuated by an AC current to sensitivity when actuated by a DC current under the same bias conditions. The DC measurements

and the E.F values are summarized in Table 4.2. Due to nonlinearities that are not considered in equations 4.3, and fabrication errors that have lowered the pull-in voltage limits of the devices E.F values are lower than ideal value $Q_m$ the mechanical quality factor of modulator beam.

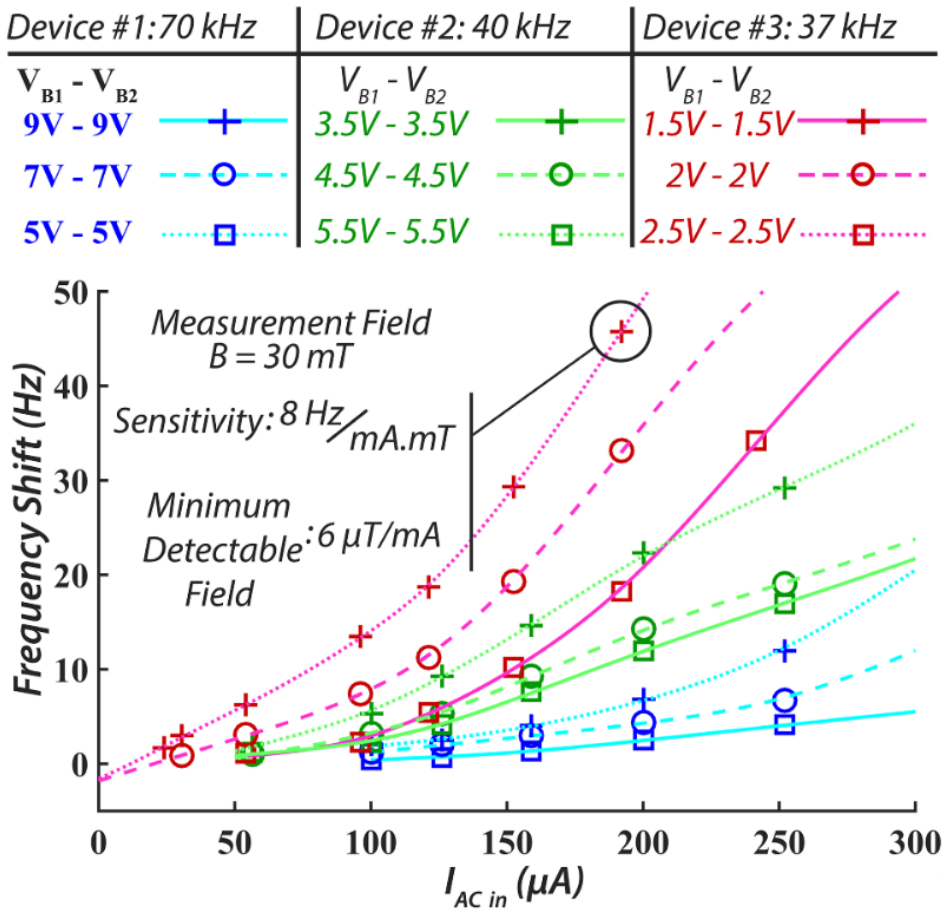


Figure 4.13. AC measurements in the presence of 30mT DC field. Frequency shifts as a function of AC Lorentz currents are plotted for all devices at various bias voltages.

Table 4.2. DC measurements and enhance factor E.F for AC measurements

| | | | | |
|---|---|---|---|---|
| **Device #1** | **$V_{B1}$, $V_{B2}$ (V)** | 7 | 9 | 10 |
| | **$I_{DC}$ (mA)** | 9.9 | 12.7 | 14.2 |
| | **$\Delta f_{DC}$ (Hz)** | 0.4 | 0.5 | 0.6 |
| | **E.F** | 2100 | 5370 | 5700 |
| **Device #2** | **$V_{B1}$, $V_{B2}$ (V)** | 3.5 | 4.5 | 5.5 |
| | **$I_{DC}$ (mA)** | 4.2 | 5.7 | 8 |
| | **$\Delta f_{DC}$ (Hz)** | 0.7 | 0.9 | 1.04 |
| | **E.F** | 450 | 650 | 1560 |
| **Device #3** | **$V_{B1}$, $V_{B2}$ (V)** | 1.5 | 2 | 2.5 |
| | **$I_{DC}$ (mA)** | 2.1 | 2.8 | 3.5 |
| | **$\Delta f_{DC}$ (Hz)** | 2.7 | 3.3 | 4.4 |
| | **E.F** | 390 | 520 | 600 |

## REFERENCES


[1] H. C. Nathanson, W. E. Newell, R. A. Wickstrom, and J. R. Davis, "The resonant gate transistor," *IEEE Transactions on Electron Devices*, vol. 14, no. 3, pp. 117–133, 1967.

[2] D. Grogg and A. M. Ionescu, "The vibrating body transistor," *IEEE Transactions on Electron Devices*, vol. 58, no. 7, pp. 2113–2121, 2011.

[3] S. T. Bartsch, A. Lovera, D. Grogg, and A. M. Ionescu, "Nanomechanical silicon resonators with intrinsic tunable gain and sub-nW power consumption," *ACS nano*, vol. 6, no. 1, pp. 256–264, 2011.

[4] W. Wang, R. Marathe, B. Bahr, L. C. Popa, and D. Weinstein, "RF solid-state vibrating transistors," in *European Frequency and Time Forum & International Frequency Control Symposium (EFTF/IFC), 2013 Joint*, 2013, pp. 529–538.

[5] A. Ansari and M. Rais-Zadeh, "A thickness-mode AlGaN/GaN resonant body high electron mobility transistor," *IEEE Transactions on Electron Devices*, vol. 61, no. 4, pp. 1006–1013, 2014.

[6] J.-S. Wenzler, T. Dunn, S. Erramilli, and P. Mohanty, "Nanoelectromechanical system-integrated detector with silicon nanomechanical resonator and silicon nanochannel field effect transistor," *Journal of Applied Physics*, vol. 105, no. 9, p. 094308, 2009.

[7] A. Rahafrooz and S. Pourkamali, "Thermal-piezoresistive energy pumps in micromechanical resonant structures," *IEEE Transactions on Electron Devices*, vol. 59, no. 12, pp. 3587–3593, 2012.

[8] V. T. Nguyen, F. Villain, and Y. L. Guillou, "Cognitive radio RF: overview and challenges," *VLSI Design*, vol. 2012, p. 1, 2012.

[9] S. Huang, X. Liu, and Z. Ding, "Opportunistic spectrum access in cognitive radio networks," in *INFOCOM 2008. The 27th Conference on Computer Communications. IEEE*, 2008, pp. 1427–1435.

[10] S. Haykin, "Cognitive radio: brain-empowered wireless communications," *IEEE journal on selected areas in communications*, vol. 23, no. 2, pp. 201–220, 2005.

[11] J. Mitola and G. Q. Maguire, "Cognitive radio: making software radios more personal," *IEEE personal communications*, vol. 6, no. 4, pp. 13–18, 1999.

[12] G. Lamontagne and A. B. Kouki, "Direct RF sampling GNSS receiver design and jitter analysis," *Positioning*, vol. 3, no. 04, p. 46, 2012.

[13] C. T.-C. Nguyen, “MEMS-based RF channel selection for true software-defined cognitive radio and low-power sensor communications,” *IEEE Communications Magazine*, vol. 51, no. 4, pp. 110–119, 2013.

[14] N. Nguyen, A. Johannessen, and U. Hanke, “Design of high-Q Thin Film Bulk Acoustic resonator using dual-mode reflection,” in *Ultrasonics Symposium (IUS), 2014 IEEE International*, 2014, pp. 487–490.

[15] T. L. Naing, T. O. Rocheleau, Z. Ren, S.-S. Li, and C. T.-C. Nguyen, “High-$ Q $ UHF Spoke-Supported Ring Resonators,” *Journal of Microelectromechanical Systems*, vol. 25, no. 1, pp. 11–29, 2016.

[16] S. Gong and G. Piazza, “Monolithic multi-frequency wideband RF filters using two-port laterally vibrating lithium niobate MEMS resonators,” *Journal of Microelectromechanical Systems*, vol. 23, no. 5, pp. 1188–1197, 2014.

[17] M. Rinaldi, C. Zuniga, C. Zuo, and G. Piazza, “Super-high-frequency two-port AlN contour-mode resonators for RF applications,” *IEEE transactions on ultrasonics, ferroelectrics, and frequency control*, vol. 57, no. 1, 2010.

[18] S. Gong, N.-K. Kuo, and G. Piazza, “GHz high-$ Q $ lateral overmoded bulk acoustic-wave resonators using epitaxial SiC thin film,” *Journal of Microelectromechanical Systems*, vol. 21, no. 2, pp. 253–255, 2012.

[19] W.-C. Li, Z. Ren, and C. T.-C. Nguyen, “A micromechanical high-Q elliptic disk displacement amplifier,” in *Micro Electro Mechanical Systems (MEMS), 2016 IEEE 29th International Conference on*, 2016, pp. 663–666.

[20] L.-W. Hung and C. T.-C. Nguyen, “Capacitive-Piezoelectric Transducers for High-$ Q $ Micromechanical AlN Resonators,” *Journal of Microelectromechanical Systems*, vol. 24, no. 2, pp. 458–473, 2015.

[21] L.-W. Hung and C. T.-C. Nguyen, “Capacitive-piezoelectric AlN resonators with Q> 12,000,” in *Micro Electro Mechanical Systems (MEMS), 2011 IEEE 24th International Conference on*, 2011, pp. 173–176.

[22] J. Segovia-Fernandez, M. Cremonesi, C. Cassella, A. Frangi, and G. Piazza, “Anchor losses in AlN contour mode resonators,” *Journal of microelectromechanical systems*, vol. 24, no. 2, pp. 265–275, 2015.

[23] A. Ansari and M. Rais-Zadeh, “Depletion-mediated piezoelectric AlGaN/GaN resonators,” *physica status solidi (a)*, vol. 213, no. 11, pp. 3007–3013, 2016.

[24] A. Ansari and M. Rais-Zadeh, “Coupled UHF Micromechanical Ring Resonators With Schottky Transducers,” *Journal of Microelectromechanical Systems*, vol. 26, no. 4, pp. 740–742, 2017.

[25] W. Thomson, “XIX. On the electro-dynamic qualities of metals:—Effects of magnetization on the electric conductivity of nickel and of iron,” *Proceedings of the Royal Society of London*, vol. 8, pp. 546–550, 1857.

[26] M. Allen, “The effect of tension on the electrical resistance of single bismuth crystals,” *Physical Review*, vol. 42, no. 6, p. 848, 1932.

[27] M. Allen, “The tension coefficients of resistance of the hexagonal crystals zinc and cadmium,” *Physical Review*, vol. 49, no. 3, p. 248, 1936.

[28] J. W. Cookson, “Theory of the piezo-resistive effect,” *Physical review*, vol. 47, no. 2, p. 194, 1935.

[29] C. S. Smith, “Piezoresistance effect in germanium and silicon,” *Physical review*, vol. 94, no. 1, p. 42, 1954.

[30] J. F. Creemer, F. Fruett, G. C. M. Meijer, and P. J. French, “The piezojunction effect in silicon sensors and circuits and its relation to piezoresistance,” *IEEE Sensors Journal*, vol. 1, no. 2, pp. 98-, Aug. 2001.

[31] H.-P. Phan, D. V. Dao, K. Nakamura, S. Dimitrijev, and N.-T. Nguyen, “The piezoresistive effect of SiC for MEMS sensors at high temperatures: a review,” *Journal of Microelectromechanical Systems*, vol. 24, no. 6, pp. 1663–1677, 2015.

[32] M. Li, H. X. Tang, and M. L. Roukes, “Ultra-sensitive NEMS-based cantilevers for sensing, scanned probe and very high-frequency applications,” *Nature nanotechnology*, vol. 2, no. 2, p. 114, 2007.

[33] L. Chen, G. H. Chen, and L. Lu, “Piezoresistive behavior study on finger-sensing silicone rubber/graphite nanosheet nanocomposites,” *Advanced Functional Materials*, vol. 17, no. 6, pp. 898–904, 2007.

[34] R. Gaska, J. W. Yang, A. D. Bykhovski, M. S. Shur, V. V. Kaminskii, and S. Soloviov, “Piezoresistive effect in GaN–AlN–GaN structures,” *Applied physics letters*, vol. 71, no. 26, pp. 3817–3819, 1997.

[35] M. Tortonese, R. C. Barrett, and C. F. Quate, “Atomic resolution with an atomic force microscope using piezoresistive detection,” *Applied physics letters*, vol. 62, no. 8, pp. 834–836, 1993.

[36] A. L. Roy and T. K. Bhattacharyya, “Design, fabrication and characterization of high performance SOI MEMS piezoresistive accelerometers,” *Microsystem Technologies*, vol. 21, no. 1, pp. 55–63, 2015.

[37] K. Matsudaira, T.-V. Nguyen, K. H. Shoji, T. Tsukagoshi, T. Takahata, and I. Shimoyama, “MEMS piezoresistive cantilever for the direct measurement of cardiomyocyte contractile force,” *Journal of Micromechanics and Microengineering*, vol. 27, no. 10, p. 105005, 2017.

[38] K. Hari, S. K. Verma, I. P. Krishna, and V. Seena, “Out-of-plane dual flexure MEMS piezoresistive accelerometer with low cross axis sensitivity,” *Microsystem Technologies*, vol. 24, no. 5, pp. 2437–2444, 2018.

[39] H. Rolnick, “Tension coefficient of resistance of metals,” *Physical review*, vol. 36, no. 3, p. 506, 1930.

[40] A. A. Barlian, W. T. Park, J. R. Mallon, A. J. Rastegar, and B. L. Pruitt, “Review: Semiconductor Piezoresistance for Microsystems,” *Proceedings of the IEEE*, vol. 97, no. 3, pp. 513–552, Mar. 2009.

[41] M. A. Hopcroft, W. D. Nix, and T. W. Kenny, “What is the Young’s Modulus of Silicon?,” *Journal of microelectromechanical systems*, vol. 19, no. 2, pp. 229–238, 2010.

[42] V. Kaajakari, “Practical MEMS: Design of microsystems, accelerometers, gyroscopes, RF MEMS, optical MEMS, and microfluidic systems,” *Las Vegas, NV: Small Gear Publishing*, 2009.

[43] G. K. Johns, “Modeling piezoresistivity in silicon and polysilicon,” *Journal of Applied Engineering Mathematics April*, vol. 2, pp. 1–5, 2006.

[44] J. C. Suhling and R. C. Jaeger, “Silicon piezoresistive stress sensors and their application in electronic packaging,” *IEEE sensors journal*, vol. 1, no. 1, pp. 14–30, 2001.

[45] S. M. Heinrich and I. Dufour, “Fundamental Theory of Resonant MEMS Devices,” *Ch*, vol. 1, pp. 3–27, 2015.

[46] A. Rahafrooz and S. Pourkamali, “High-frequency thermally actuated electromechanical resonators with piezoresistive readout,” *IEEE Transactions on Electron Devices*, vol. 58, no. 4, pp. 1205–1214, 2011.

[47] Z. Gniazdowski and P. Kowalski, “Practical approach to extraction of piezoresistance coefficient,” *Sensors and Actuators A: Physical*, vol. 68, no. 1–3, pp. 329–332, 1998.

[48] S. I. Kozlovskiy and I. I. Boiko, “First-order piezoresistance coefficients in silicon crystals,” *Sensors and Actuators A: Physical*, vol. 118, no. 1, pp. 33–43, 2005.

[49] C.-H. Cho, R. C. Jaeger, and J. C. Suhling, “Characterization of the Temperature Dependence of the Piezoresistive Coefficients of Silicon” *IEEE Sensors Journal*, vol. 8, no. 8, pp. 1455–1468, 2008.

[50] V. Cimalla, J. Pezoldt, and O. Ambacher, “Group III nitride and SiC based MEMS and NEMS: materials properties, technology and applications,” *Journal of Physics D: Applied Physics*, vol. 40, no. 20, p. 6386, 2007.

[51] J. S. Shor, L. Bemis, and A. D. Kurtz, “Characterization of monolithic n-type 6H-SiC piezoresistive sensing elements,” *IEEE Transactions on Electron Devices*, vol. 41, no. 5, pp. 661–665, 1994.

[52] A. D. Bykhovski, V. V. Kaminski, M. S. Shur, Q. C. Chen, and M. A. Khan, “Piezoresistive effect in wurtzite n-type GaN,” *Applied physics letters*, vol. 68, no. 6, pp. 818–819, 1996.

[53] M. A. Fraga, R. S. Pessoa, H. S. Maciel, and M. Massi, “Recent developments on silicon carbide thin films for piezoresistive sensors applications,” in *Silicon Carbide-Materials, Processing and Applications in Electronic Devices*, InTech, 2011.

[54] B. van der Schoot, M. Boillat, and N. de Rooij, “Micro-instruments for life science research,” *IEEE Transactions on Instrumentation and Measurement*, vol. 50, no. 6, pp. 1538–1542, Dec. 2001.

[55] K. A. Makinwa and J. H. Huijsing, “A smart wind sensor using thermal sigma-delta modulation techniques,” *Sensors and Actuators A: Physical*, vol. 97, pp. 15–20, 2002.

[56] S. Park, S. Kim, S. Kim, and Y. Kim, “A flow direction sensor fabricated using MEMS technology and its simple interface circuit,” *Sensors and Actuators B: Chemical*, vol. 91, no. 1–3, pp. 347–352, 2003.

[57] X. Chen and A. Lal, “Integrated pressure and flow sensor in silicon-based ultrasonic surgical actuator,” in *Ultrasonics Symposium, 2001 IEEE*, 2001, vol. 2, pp. 1373–1376.

[58] J. Kang, Y. Kim, H. Kim, J. Jeong, and S. Park, “Comfort sensing system for indoor environment,” in *Solid State Sensors and Actuators, 1997. TRANSDUCERS’97 Chicago., 1997 International Conference on*, 1997, vol. 1, pp. 311–314.

[59] N. T. Nguyen, “Micromachined flow sensors—a review,” *Flow measurement and Instrumentation*, vol. 8, no. 1, pp. 7–16, 1997.

[60] S. Beeby, G. Ensel, and M. Kraft, *MEMS mechanical sensors*. Artech House, 2004.

[61] S. D. Nguyen, I. Paprotny, P. K. Wright, and R. M. White, “In-plane capacitive MEMS flow sensor for low-cost metering of flow velocity in natural gas pipelines,” in *Micro*

*electro mechanical systems (MEMS), 2014 IEEE 27th International Conference on*, 2014, pp. 971–974.

[62] Y.-H. Wang, C.-Y. Lee, and C.-M. Chiang, "A MEMS-based air flow sensor with a free-standing micro-cantilever structure," *Sensors*, vol. 7, no. 10, pp. 2389–2401, 2007.

[63] N. Svedin, E. Kälvesten, E. Stemme, and G. Stemme, "A lift-force flow sensor designed for acceleration insensitivity," *Sensors and Actuators A: Physical*, vol. 68, no. 1–3, pp. 263–268, 1998.

[64] R. H. OlssonIII, K. E. Wojciechowski, M. S. Baker, M. R. Tuck, and J. G. Fleming, "Post-CMOS-compatible aluminum nitride resonant MEMS accelerometers," *Journal of Microelectromechanical Systems*, vol. 18, no. 3, pp. 671–678, 2009.

[65] A. L. Herrera-May, L. A. Aguilera-Cortés, P. J. García-Ramírez, and E. Manjarrez, "Resonant magnetic field sensors based on MEMS technology," *Sensors*, vol. 9, no. 10, pp. 7785–7813, 2009.

[66] M. J. Thompson and D. A. Horsley, "Resonant MEMS magnetometer with capacitive read-out," in *Sensors, 2009 IEEE*, 2009, pp. 992–995.

[67] P. Thiruvenkatanathan, J. Yan, J. Woodhouse, and A. A. Seshia, "Enhancing parametric sensitivity in electrically coupled MEMS resonators," *Journal of Microelectromechanical Systems*, vol. 18, no. 5, pp. 1077–1086, 2009.

[68] P. Thiruvenkatanathan, J. Yan, J. Woodhouse, A. Aziz, and A. A. Seshia, "Ultrasensitive mode-localized mass sensor with electrically tunable parametric sensitivity," *Applied Physics Letters*, vol. 96, no. 8, p. 081913, 2010.

[69] C. Zhao, G. S. Wood, J. Xie, H. Chang, S. H. Pu, and M. Kraft, "A three degree-of-freedom weakly coupled resonator sensor with enhanced stiffness sensitivity," *Journal of Microelectromechanical Systems*, vol. 25, no. 1, pp. 38–51, 2016.

[70] H. Zhang, B. Li, W. Yuan, M. Kraft, and H. Chang, "An acceleration sensing method based on the mode localization of weakly coupled resonators," *Journal of microelectromechanical systems*, vol. 25, no. 2, pp. 286–296, 2016.

[71] S. Pourkamali and F. Ayazi, "Electrically coupled MEMS bandpass filters: Part I: With coupling element," *Sensors and Actuators A: Physical*, vol. 122, no. 2, pp. 307–316, 2005.

[72] S. Pourkamali, A. Hashimura, R. Abdolvand, G. K. Ho, A. Erbil, and F. Ayazi, "High-Q single crystal silicon HARPSS capacitive beam resonators with self-aligned sub-100-nm transduction gaps," *Journal of Microelectromechanical Systems*, vol. 12, no. 4, pp. 487–496, 2003.

## BIOGRAPHICAL SKETCH

Alireza Ramezany was born in Tehran, Iran. In 2008, he started his undergraduate studies at the Sharif University of Technology in Electrical Engineering with a focus on electronic circuits and devices. In 2013, he joined the Micronexlab at The University of Texas at Dallas to pursue his direct Ph.D. degree under the supervision and guidance of Dr. Siavash Pourkamali. During his Ph.D., he took part in a variety of projects related to micro/nanoelectromechanical systems that employed capacitive, thermal, and piezoelectric actuation mechanisms. His specialties include RF-MEMS filters, piezoelectric-on-silicon resonators, sensors with capacitive transduction, and thermal actuators. His dissertation focused on piezoresistive internal amplification in resonant devices as a viable frequency selective signal amplification mechanism.

# CURRICULUM VITAE

**Alireza Ramezany**
Email: e.ramezany@utdallas.edu

**PhD candidate** in Electrical Engineering, specialized in design, fabrication, and characterization of **RF NEMS/MEMS** at The University of Texas at Dallas under guidance of Dr. Siavash Pourkamali. Main projects include **Nanoscale Thermal Piezoresistive, Thin Film Piezoelectric on silicon (Aluminum Nitride), and Capacitive Resonators**.

## EDUCATION

**Direct PhD in Electrical Engineering** **Aug 2013-July 2018**
**The University of Texas at Dallas**
**Thesis: Nano-Electromechanical Active Resonant Devices**
The goal of this dissertation was to achieve active RF Nano and Microscale Electromechanical Resonators that can offer narrow band filtering and signal amplification without the need for solid state technology though the novel concept of internal amplification. Such devices absorb power from a DC source and through an internal electromechanical feedback achieve much higher vibration amplitudes at resonance. **Resonant Thermal Piezoresistive Amplifiers:** Design and fabrication of thermally actuated UHF I-Bar resonators with $<1\mu m^2$ footprint using E-Beam lithography on thin SOI substrates to demonstrate the internal amplification, High quality factors, and power gains at ultra-high frequencies(>0.3GHz). Under this study, such devices have shown very large quality factors with minimal to no insertion loss at 750MHz.

**Graduation Date:** **July 2018**

**Courses:**
Fields and Waves, Quantum Physical Electronics, Active Semiconductor Devices, Introduction to MEMS, Electronic Optical and Magnetic materials, Lithography and Nanofabrication, Semiconductor Processing Technology, Analog Integrated Circuit Design, Digital Signal Processing. GPA: 3.703

**Bachelor's in Electrical Engineering** **June 2013**
**Sharif University of Technology**, Tehran, Iran
**Final Project:** Implementation of a system to measure critical current of a thin film superconductor using 3rd harmonic voltage
Other projects: Theoretical Design of a low supply voltage rail-to- rail operational Amplifier, Design of a BP filter with tunable frequency margin

**Relevant Courses:** Advanced Solid-State Physics, Applied Quantum Mechanics, Analog/RF Circuit Design

## Research Experience

**The University of Texas at Dallas** **Aug 2013-present**
**Projects Under Supervision of Dr. Siavash Pourkamali**

- Characterization of **Thin-Film Piezoelectric(AlN) on Silicon Resonators** as gas flow sensors and frequency output Force Probes.
- Study of **Anchor loss** in Thermal Piezoresistive and Piezoelectric Piezoresistive Amplifiers using **FEM analysis and perfectly matched layers**.
- Micro-fabrication of thin **Aluminum Nitride on SOI substrate** using a six-mask process.
- Design, fabrication, and characterization of **weakly Coupled Capacitive Resonators using Doubly-clamped silicon Beams** for sensory applications.
- Design, FEM Simulation, and Measurement of **VLF PZT Lateral Bulk Resonators (<30kHz)** as Mechanical Antennas.
- Design and Fabrication of novel **Electrostatic Motors using silicon substrates with improved specific torque density**.
- Design and FEM Simulation of Thermal Piezoresistive Amplifiers as **chip-scale circulators for signal processing at RF**.
- Development of a new electromechanical model for Thermal Piezoresistive Amplifiers.
- Implementation and development of a **self-aligned multi-layer fabrication process using E-Beam lithography** for the first time in the research group.
- Design and development of CMOS compatible MEMS resonators in collaboration with Texas Instruments.
- Design and fabrication of Electromechanical Tunneling Transistors using E-Beam lithography.
- Characterization of Digitally Operated MEMS rotational accelerometers.

## SKILLS AND TECHNIQUES

**Cleanroom Experience:** Photolithography, E-beam evaporation and sputtering, Plasma etch (ICP and DRIE), SEM, E-Beam lithography, and ALD.
**Characterization Experience**: wire-bonding (wedge and ball bonding), RF probe station, RF PCB design, Network analysis and calibration (including SLOT and TRL), Spectrum analysis (including Noise figure and phase noise measurements)
**Software:** COMSOL MEMS Module, Cadence, Pspice, Matlab, C/C++**,** L-Edit, and Solid Works

## PUBLICATIONS

**Journal Papers:**

1. **Ramezany, A,** and Siavash Pourkamali." Ultra-High frequency nanomechanical Piezoresistive Amplifiers for Direct Channel-Selective Front-Ends". Nano Letters (2018) (Under Review).
2. **Ramezany, A**, Mahdavi, M, and Pourkamali, S. "Nanoelectromechanical resonant narrow-band amplifiers." **Nature** *Microsystems & Nanoengineering* 2 (2016): 16004.
3. Kumar, V., **Ramezany, A**., Mahdavi, M., & Pourkamali, S. (2016). Amplitude modulated Lorentz force MEMS magnetometer with picotesla sensitivity. *Journal of Micromechanics and Microengineering*, *26*(10), 105021.
4. Mahdavi, M., Abbasalipour, A.**, Ramezany, A**., & Pourkamali, S. (2016). Micromachined Frequency-Output Force Probes. *IEEE Sensors Journal*, *16*(14), 5520-5521.

**Conference Papers:**

1. **Ramezany, A**., Babu, S., Kumar, V., Lee, J. B., & Pourkamali, S. (2017, January). Resonant piezoresistive amplifiers: Towards single element nano-mechanical RF front ends. In *Micro Electro Mechanical Systems (MEMS), 2017 IEEE 30th International Conference on* (pp. 72-75). IEEE.
2. **Ramezany, A**., Mahdavi, M., Moses, A., & Pourkamali, S. (2015, June). Sail-shaped piezoelectric micro-resonators for high resolution gas flowmetry. In *Solid-State Sensors, Actuators and Microsystems (TRANSDUCERS), 2015 Transducers-2015 18th International Conference on* (pp. 2252-2255). IEEE.
3. **Ramezany, A**., Qaradaghi, V., Kumar, V., & Pourkamali, S. (2016, October). Frequency modulated electrostatically coupled resonators for sensing applications. In *SENSORS, 2016 IEEE* (pp. 1-3). IEEE.
4. Mahdavi, **M., Ramezany**, A., Kumar, V., & Pourkamali, S. (2015, January). SNR improvement in amplitude modulated resonant MEMS sensors via thermal-piezoresistive internal amplification. In *Micro Electro Mechanical Systems (MEMS), 2015 28th IEEE International Conference on* (pp. 913-916). IEEE.
5. Guo, X., Mehdizadeh, E., Kumar, V., **Ramezany, A**., & Pourkamali, S. (2014, November). An ultra-high Q micromechanical in-plane tuning fork. In *SENSORS, 2014 IEEE* (pp. 990-993). IEEE.
6. Kumar, V., **Ramezany, A.**, Mazrouei, S., Jafari, R., & Pourkamali, S. (2017, January). A 3-bit digitally operated MEMS rotational accelerometer. In *Micro Electro Mechanical Systems (MEMS), 2017 IEEE 30th International Conference on* (pp. 1087-1090). IEEE.
7. Qaradaghi, V., Mahdavi, M., **Ramezany, A**., & Pourkamali, S. (2016, May). MEMS resonant sensors for real-time thin film shear stress monitoring. In *Frequency Control Symposium (IFCS), 2016 IEEE International* (pp. 1-4). IEEE.

**8.** Mahdavi, M., **Ramezany, A**., Ravi, H., & Pourkamali, S. (2016, May). An analog micro-electromechanical XOR. In *Frequency Control Symposium (IFCS), 2016 IEEE International* (pp. 1-4). IEEE.